frontiers in Earth Science

ORIGINAL RESEARCH
published: 11 May 2021
doi: 10.3389/feart.2021.657618

Petrogenesis, Redox State, and Mineralization Potential of Triassic Granitoids in the Mengshan District, South China

Yanshen Yang[1,2], Xiaofei Pan[2], Zengqian Hou[2], Yang Deng[2], Yongpeng Ouyang[3], Delei Meng[3] and Tao Xie[3]*

[1] School of Earth Sciences and Resources, China University of Geosciences, Beijing, China, [2] Institute of Geology, Chinese Academy of Geological Sciences, Beijing, China, [3] 912 Geological Team, Bureau of Geology and Mineral Resources of Jiangxi Province, Yingtan, China

OPEN ACCESS

Edited by:
Guoguang Wang, Nanjing University, China

Reviewed by:
Jinxiang Li, Key Laboratory of Continental Collision and Plateau Uplift, Institute of Tibetan Plateau Research Chinese Academy of Sciences (CAS), China
Renzhi Zhu, Northwest University, China
Jingjing Zhu, Institute of Geochemistry Chinese Academy of Sciences (CAS), China
Huan Li, Central South University, China
Shiyong Liao, Purple Mountain Observatory Chinese Academy of Sciences (CAS), China

***Correspondence:**
Xiaofei Pan
pan_smile0551@sina.com

Specialty section:
This article was submitted to Economic Geology, a section of the journal Frontiers in Earth Science

Received: *23 January 2021*
Accepted: *06 April 2021*
Published: *11 May 2021*

Citation:
Yang Y, Pan X, Hou Z, Deng Y, Ouyang Y, Meng D and Xie T (2021) Petrogenesis, Redox State, and Mineralization Potential of Triassic Granitoids in the Mengshan District, South China. Front. Earth Sci. 9:657618. doi: 10.3389/feart.2021.657618

The Mengshan district is located in the eastern segment of the Jiangnan Orogen in South China. Multi-phase intrusions were emplaced in this district, with the medium-grained porphyritic biotite granite and its marginal phase (fine-grained porphyritic biotite granite) genetically related to metal and non-metal mineralization. In this study, zircon U–Pb ages and trace elements, whole-rock geochemistry, and Nd isotopes were systematically analyzed for medium- and fine-grained porphyritic biotite granite in the Mengshan district, with the aim of elucidating the origin, evolutionary process, redox state, and mineralization competency of the studied granites. The Laser Ablation Inductively Coupled Plasma Mass Spectrometry (LA–ICP–MS) zircon U–Pb dating provided a weighted mean age of 226.6 ± 0.5 to 225.9 ± 0.5 Ma for the studied Mengshan granites, synchronous with the late-episode Triassic magmatism-mineralization in South China. The studied Mengshan granites are high-Si and -K, low-P, and weakly peraluminous, exhibiting features of highly evolved I-type granites. The detailed whole-rock geochemistry and Nd isotopes, and zircon trace elements and Hf isotopes demonstrated that the studied Mengshan granites were likely derived from disequilibrium melting of Proterozoic metamorphic basements that were composed of meta-igneous and metasediments and underwent fractional crystallization of plagioclase, K-feldspar, biotite, Fe-Ti oxide, zircon, and apatite. Low whole-rock K/Rb (<150), Nb/Ta (<6), and Zr/Hf (<26) ratios and the metasomatized rim of zircon also suggest that the melt–fluid interaction occurred during the formation of more evolved fine-grained porphyritic biotite granite. The Mengshan granites have a relatively reduced redox state, revealed by their relatively low whole-rock Fe_2O_3/FeO ratios (mostly < 0.5), zircon Ce^{4+}/Ce^{3+} ratios (mostly lower than 90), and oxygen fugacity (below ΔFMQ + 1.4). The data in this study indicate that the Mengshan granites, especially the more evolved fine-grained porphyritic biotite granite, are favorable for W, Sn, Mo (<0.3 Mt), and Cu (<1 Mt) mineralization. Moreover, the contact zone between the fine-grained porphyritic biotite granite (or other Triassic granites) and the Permian Maokou Formation (flint-nodule limestone) is a potential target region for wollastonite exploration.

Keywords: Mengshan, Jiangnan Orogen, Triassic, I-type granite, oxygen fugacity, mineralization

INTRODUCTION

Granites are the most important component of the continental crust (e.g., Chen and Grapes, 2007; Brown, 2013; Wang, 2017) and are tightly associated with various magmatic-hydrothermal ore deposits (e.g., Hua and Mao, 1999; Černý et al., 2005; Chen et al., 2008). In most cases, granites are the dominant source of ore deposits. However, owing to the varying source composition, melting conditions, crystallization paths, wall-rock assimilation, and melt–fluid interaction, the compositions of the granites are variable, leading to different mineralization competencies (Černý et al., 2005). Therefore, research works on the petrogenesis and mineralization competencies of the ore-bearing granitoids are crucial, which can make it easier to discriminate the ore-bearing granites that are related to different types of mineralization. Generally, the Sn, W, and rare-metal deposits are closely associated with highly evolved and reduced granites, whereas the Cu, Mo, and Au deposits are related to the less-evolved and oxidized granites (e.g., Hedenquist and Lowenstern, 1994; Jiang et al., 2020).

Mesozoic magmatism is vastly distributed in South China (e.g., Sun et al., 2003; Sun, 2006; Zhou et al., 2006). Owing to its tectonic significances and its close relationship with large-scale non-metal and polymetallic mineralization, Mesozoic magmatism has been extensively studied (e.g., Wang et al., 2002, 2007, 2013; Hou et al., 2013; Li C. L. et al., 2021; Ni et al., 2021). Previous research divided the ore deposits of the Mesozoic ages into three episodes (Mao et al., 2013): the Late Triassic (230–210 Ma), Early–Late Jurassic (170–150 Ma), and Early–Mid Cretaceous (120–80 Ma). Among these, the Jurassic–Cretaceous magmatism-mineralization is more extensive and has received more attention, whereas research on the Triassic one is relatively lesser. In recent years, a series of Triassic ore deposits, e.g., the Limu W–Sn–Nb–Ta (Yang et al., 2009), Tianmuchong W–Sn (Du et al., 2015), Hehuaping Sn (Cai et al., 2006), and Nanyangtian W deposit (Feng et al., 2011), have been recognized, which has attached an increasing interest in the study of Triassic magmatism and its related mineralization.

The Mengshan district is located in the eastern segment of the Jiangnan Orogen in South China (**Figure 1**). This district has the largest ancient silver mining relics in Asia, dating back to the Yuan Dynasty in the 12th century. Because many ore deposits have been rediscovered by tracing ancient mining relicts, including the Dexing Cu–Mo–Au and Gejiu Sn deposits (Zhu et al., 1983; Cheng and Mao, 2010), detailed geological and geochemical surveys at scales of 1:200,000 and 1:50,000 have been performed in the Mengshan district (Jiangxi Bureau of Geology and Mineral Resources [Jiangxi BGMR], unpublished). These surveys revealed extensive magmatism and hydrothermal alteration in the area. The petrological features of the igneous rocks and the relationships between these igneous rocks were also well defined. However, because of the limitation in geochronological methods, the ages of granites in the Mengshan district were recognized to be Jurassic (ca. 170 Ma; Jiangxi Bureau of Geology and Mineral Resources [Jiangxi BGMR], unpublished). Zhong et al. (2011) re-dated the Mengshan granites using the Laser Ablation Inductively Coupled Plasma Mass Spectrometry (LA–ICP–MS) zircon U–Pb method, demonstrating that these granites were emplaced during the Triassic (ranging from 236 to 217 Ma). In recent years, the largest wollastonite deposit in the world and several small to medium ore deposits have been found in this district, with the geological characteristics of these ore deposits being well defined (You et al., 2006; Chen et al., 2018; Xiao and Yu, 2019; Wang et al., 2019). However, the petrogenesis of the ore-bearing granites and the possible connections between these granites and mineralization remain unclear. In this study, we carried out U–Pb age, trace element, and Hf isotope analyses of zircons from the ore-bearing granites in the Mengshan district, as well as the whole-rock geochemistry and Nd isotopes. These studies aim to investigate the emplacement ages, petrogenesis, and redox states of the ore-bearing granites. Combined with published geochronological and zircon trace elemental data, this study also attempts to identify the mineralization potential of the ore-bearing granites.

GEOLOGY OF THE MENGSHAN DISTRICT

District Geology

The Mengshan district is located in western Jiangxi Province, within the interior of South China (**Figure 1**). Geologically, it is located in the southern part of the Jiangnan Orogen (**Figure 1**) and is adjacent to the Jiuling thrust in the north and the Wugongshan metamorphic core complex in the south (Wang et al., 2019). This district is largely influenced by the Triassic and Jurassic–Cretaceous orogeny. The Triassic orogeny formed the general tectonic framework of the Mengshan district, featuring NE- and NEE-trending folding of Late Paleozoic (Carboniferous to Permian) littoral strata, NW-trending transtensional fracture, angle unconformity in the Late Permian to Early Jurassic strata, and intrusions of the Mengshan granitic complex (Jiangxi Bureau of Geology and Mineral Resources [Jiangxi BGMR], unpublished; **Figure 2**). The Jurassic–Cretaceous orogeny reformed the Triassic fold and resulted in NE-trending compressional fractures and a series of igneous veins and dikes (Jiangxi Bureau of Geology and Mineral Resources [Jiangxi BGMR], unpublished; **Figure 2**).

The exposed stratum in the Mengshan district mainly comprises the Carboniferous Huanglong, Permian Qixia and Maokou, and Leping Formation (**Figure 2**). The Huanglong Formation comprises limestone, dolostone, and dolomite limestone. The Qixia Formation comprises crystalline limestone, bioclastic limestone, argillaceous limestone, dolomite limestone, and carbonaceous mudstone. The Permian Maokou Formation comprises crystalline limestone, flint-nodule limestone, and carbonaceous mudstone, and the Leping Formation comprises sandstone, shale, and carbonaceous mudstone.

Igneous Petrology

Influenced by Triassic and Jurassic–Cretaceous tectonic events, multiple periods of magmatism occurred in the Mengshan district and formed the Mengshan complex, which is settled in the central part of the Mengshan district, with an exposure area of 39 km^2 (**Figure 2**). This complex is mainly composed of Triassic

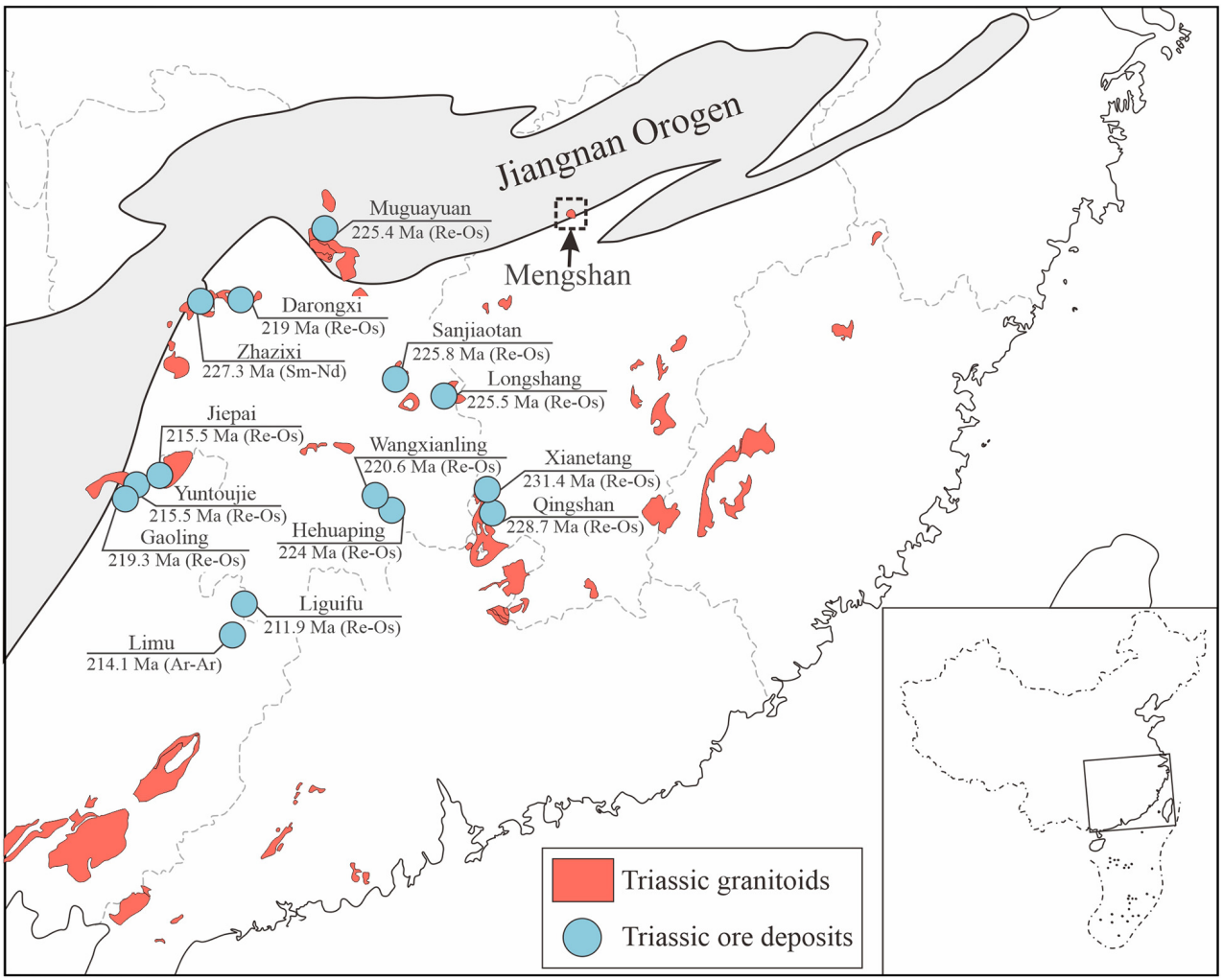

FIGURE 1 | Simplified geological map of South China, showing the distribution of Triassic granitoids (modified after Sun, 2006).

granites and Jurassic–Cretaceous dikes, and the distribution of these igneous rocks and their detailed occurrences and lithologies will be introduced in the following sections.

Triassic Granitic Magmatism

The Triassic granitic magmatism is the largest and most important magmatism in the Mengshan district, and these granites constitute the main body of the Mengshan complex (**Figure 2**). Based on previous studies (Jiangxi Bureau of Geology and Mineral Resources [Jiangxi BGMR], unpublished; Zhong et al., 2011), the Mengshan Triassic granites can be divided into three stages. The first-stage granites constitute the main body of the Mengshan complex (71%) and can be further subdivided into two phases: the transitional and marginal phases (Jiangxi Bureau of Geology and Mineral Resources [Jiangxi BGMR], unpublished). The transitional phase is composed of medium-grained porphyritic biotite granite (**Figures 3A,B**). It generally consists of quartz, K-feldspar, plagioclase, and a few biotites as phenocrysts (30%–40%) up to 3 cm in length in a medium- to fine-grained groundmass of quartz, K-feldspar, plagioclase, and biotite. The marginal phase is composed of fine-grained porphyritic biotite granite (**Figures 3C,D**) and generally consists of medium- to coarse-grained K-feldspar, quartz, and plagioclase as phenocrysts (20–25%) and quartz, K-feldspar, plagioclase, and biotite as the fine-grained matrix. Based on the fieldwork, there is no distinct interface between these two phases of granites (Jiangxi Bureau of Geology and Mineral Resources [Jiangxi BGMR], unpublished), indicating a transitional relationship. Notably, an intense greisen and potassic alteration developed in the apical zone of the fine-grained porphyritic biotite granite, with the skarn alteration developed in the contact zone between the granite and carbonate rocks (**Figures 4A–F**), indicating that the fine-grained porphyritic biotite granite is closely related to alteration and mineralization in the Mengshan district. The second-stage granite is composed of fine-grained porphyritic biotite granite and comprises 5–10% coarse-grained K-feldspar as the phenocrysts and fine-grained quartz, K-feldspar, plagioclase, and biotite as the matrix. The third-stage granite is composed

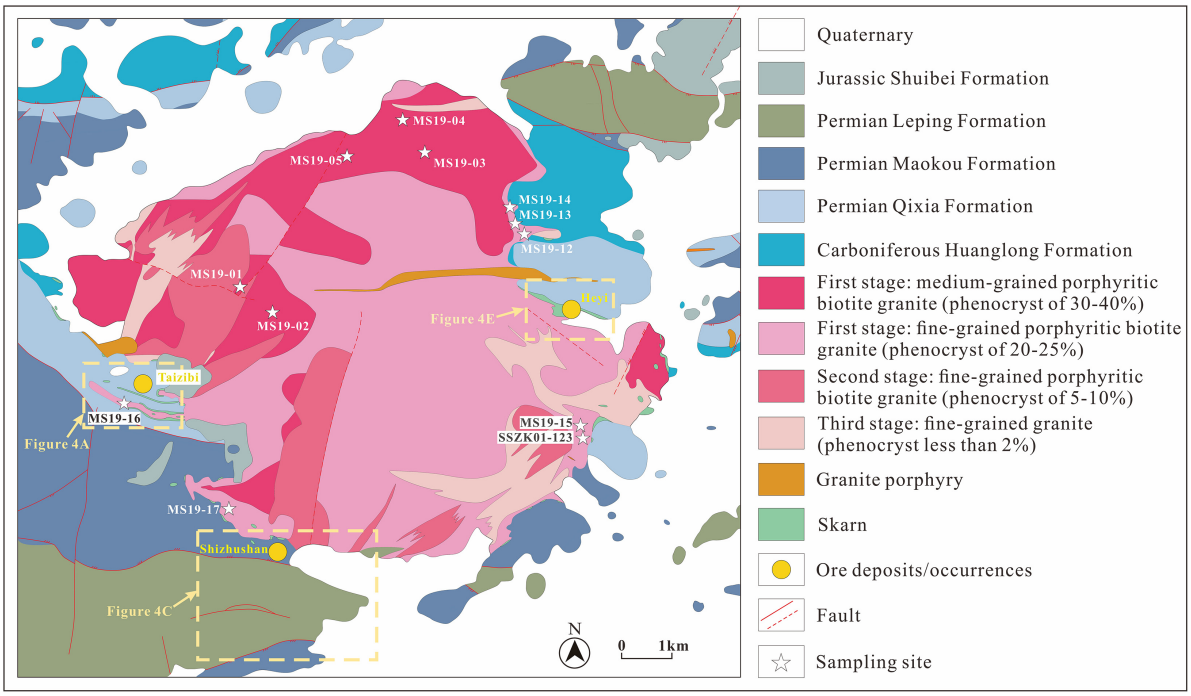

FIGURE 2 | Geological map of Mengshan district (modified after Jiangxi Bureau of Geology and Mineral Resources [Jiangxi BGMR], unpublished).

of fine-grained granite and consists of less than 2% medium- to coarse-grained K-feldspar as phenocrysts and the fine-grained matrix of quartz, K-feldspar, plagioclase, and biotite. The second- and third-stage granites intruded into the first-stage granites with distinct boundaries (**Figure 3F**; Jiangxi Bureau of Geology and Mineral Resources [Jiangxi BGMR], unpublished), indicating that they occurred as later intrusions.

Accessory minerals in the Mengshan Triassic granites include zircon, apatite, monazite, scheelite, and fluorite. The zircons occur as inclusions in biotites or as interstitial minerals among rock-forming minerals. The monazites mostly occur as inclusions in feldspars, and the apatites mostly occur as inclusions in biotite. In particular, fluorite was found as inclusions in K-feldspar in the first-stage fine-grained porphyritic biotite granite. Fluorite, showing no signs of alteration or veinlets cutting around them, has directly grown in the rock-forming minerals (**Figure 3E**), indicating that the granitic system is rich in fluorine.

Jurassic–Cretaceous Magmatism

Jurassic–Cretaceous igneous rocks, which intruded as veins and dikes crosscutting the Triassic granites and the surrounding sedimentary rocks (**Figures 2**, **5A**), are also found in the Mengshan district. These vein rocks predominantly include granite porphyry (142.1 ± 0.8 Ma; unpublished data) and diorite porphyry (135.3 ± 0.2 Ma; unpublished data). The granite porphyry mostly outcrops in the eastern part of the Mengshan district (**Figure 2**), whereas the diorite porphyry mostly outcrops in the western part of Mengshan district (**Figure 5A**).

ALTERATION AND MINERALIZATION IN THE MENGSHAN DISTRICT

Based on previous studies and the detailed field observations recorded by the authors of this paper in the Mengshan district, there are several ore deposits/occurrences in the Mengshan district. The geological characteristics of the representative Taizibi, Shizhushan, and Heyi deposits are described below.

Taizibi Deposit

Taizibi deposit is a medium-sized Sn-polymetallic deposit (Jiangxi Bureau of Geology and Mineral Resources [Jiangxi BGMR], unpublished) that is found in the western part of the Mengshan complex (**Figure 2**). This deposit contains a total of 31 ore bodies and 20,708 t of SnO_2 (Jiangxi Bureau of Geology and Mineral Resources [Jiangxi BGMR], unpublished). The exposed strata of this district include the Permian Qixia and Maokou Formation and Quaternary sediments. The intrusions in the Taizibi district are simple and composed of fine-grained porphyritic biotite granite and diorite porphyry. The fine-grained porphyritic biotite granite intruded as stocks and apophyses into the carbonate rocks of the Permian Qixia Formation (**Figures 5A,B**), whereas the diorite porphyry intruded as small dikes into the fine-grained porphyritic biotite granite and the carbonate rocks of the Permian Qixia Formation (**Figures 5A,B**). The main geological structure of the Taizibi district includes a series of NWW- and NNE-trending faults. The NWW-trending faults are the most important faults in the district

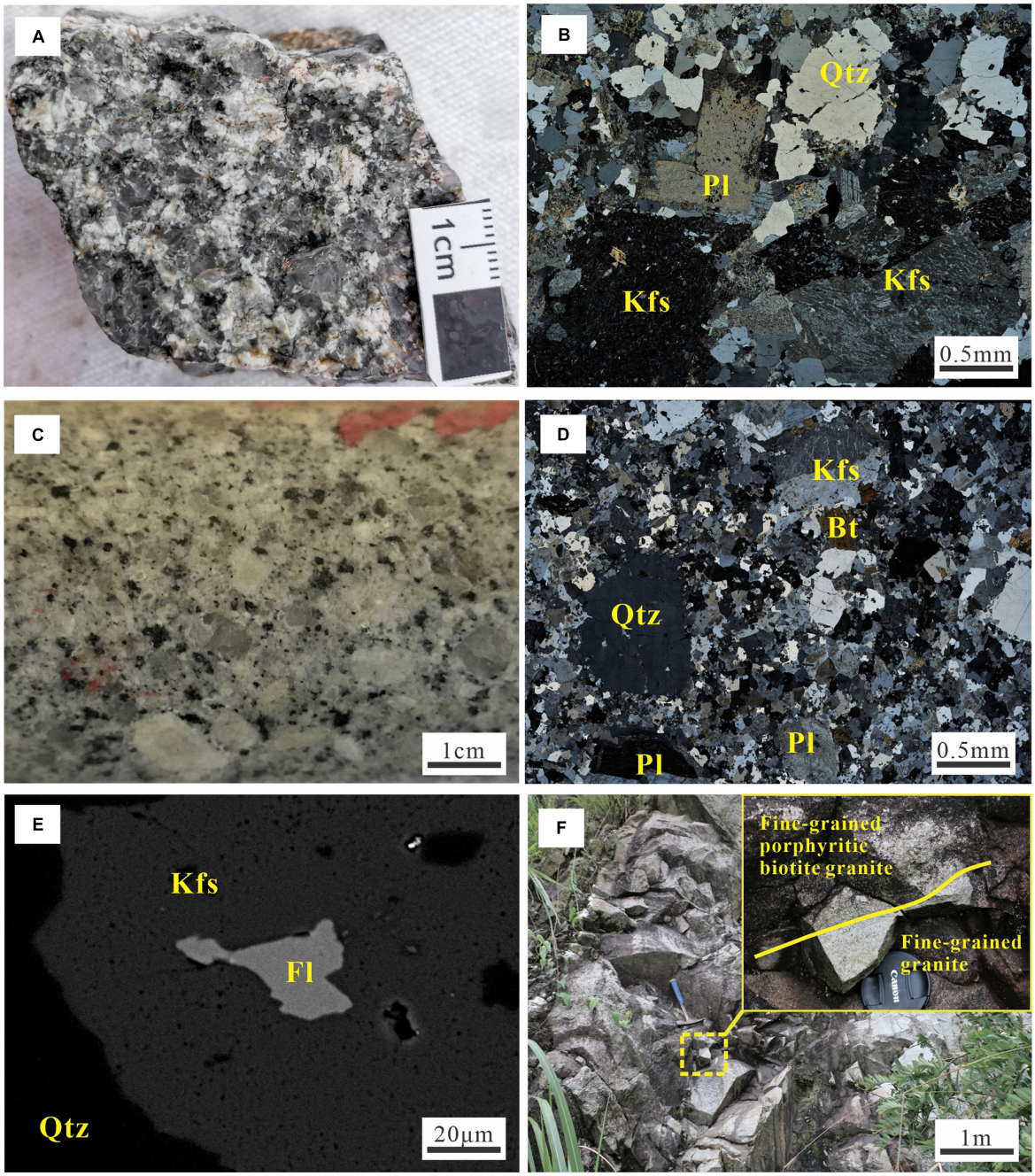

FIGURE 3 | Petrographical characteristics of the studied Mengshan granites. **(A)** Hand specimen of the medium-grained porphyritic biotite granite; **(B)** Photomicrograph of the medium-grained porphyritic biotite granite; **(C)** Hand specimen of the fine-grained porphyritic biotite granite; **(D)** Photomicrograph of the fine-grained porphyritic biotite granite; **(E)** Back-scattered electron (BSE) image of the fine-grained porphyritic biotite granite, showing that the fluorite occurs as inclusion in the K-feldspar; **(F)** The fine-grained granite (the third stage) intruded into the fine-grained porphyritic biotite granite (the first stage). Symbols: Pl, plagioclase; Kfs, K-feldspar; Qtz, quartz; Bt, biotite; Fl, fluorite.

because they control not only the emplacement of the fine-grained porphyritic biotite granite but also the distribution of the alteration and mineralization (Jiangxi Bureau of Geology and Mineral Resources [Jiangxi BGMR], unpublished). The NNE-trending faults crosscut the fine-grained porphyritic biotite granite and skarn, suggesting that they were post-mineralization faults (**Figure 5A**).

The Sn-polymetallic mineralization primarily occurs in the contact zone (garnet–diopside skarn) between the fine-grained porphyritic biotite granite and the Permian Qixia Formation, with minor amounts in the altered granite (Jiangxi Bureau of Geology and Mineral Resources [Jiangxi BGMR], unpublished). The ore minerals mainly include cassiterite, stannite, chalcopyrite, bornite, and scheelite. In addition,

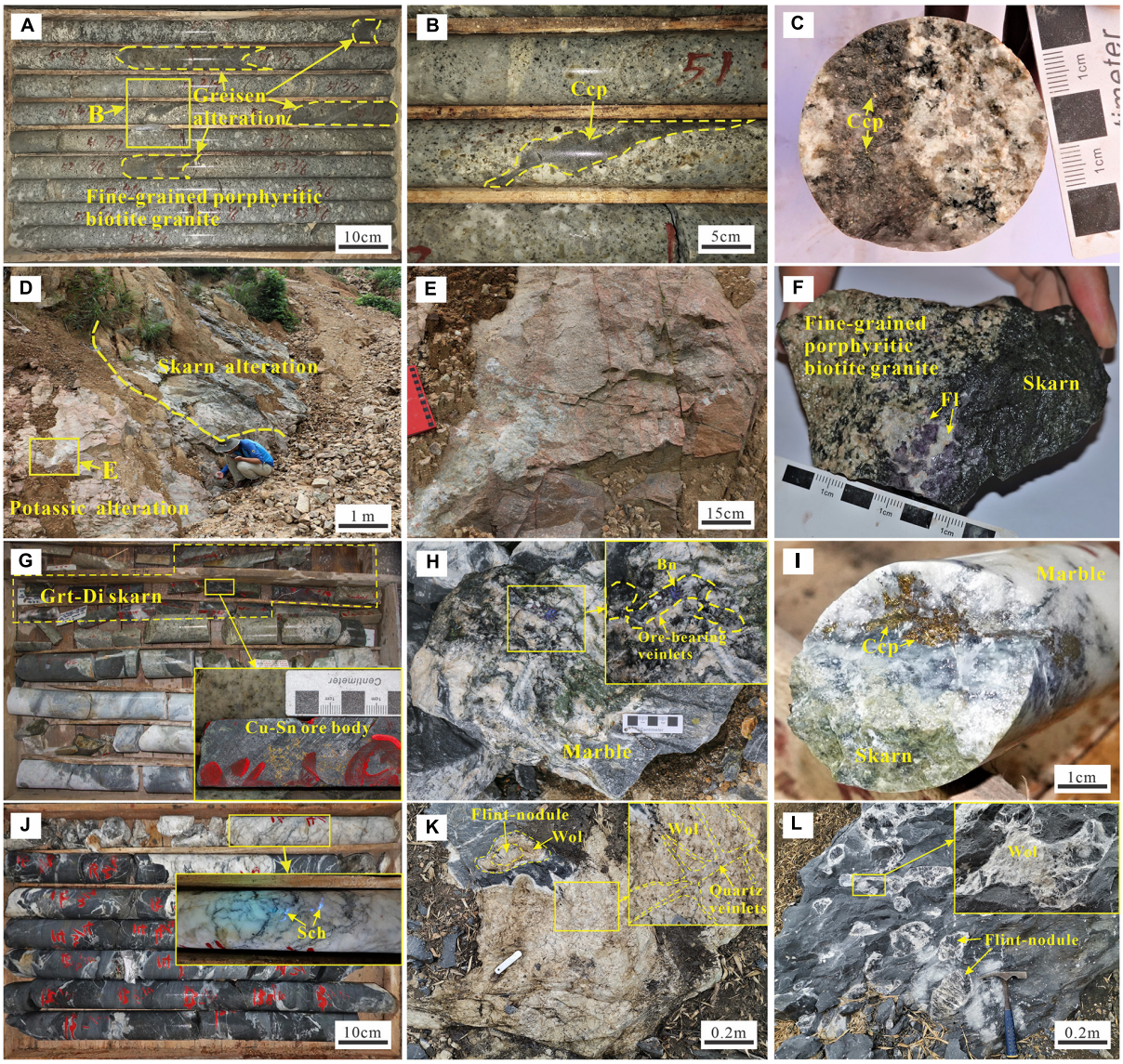

FIGURE 4 | Alteration and mineralization features in the Mengshan district. **(A–C)** Greisen alteration in the fine-grained porphyritic biotite granite and its related veinlet Cu mineralization; **(D,E)** Potassic alteration developed in the apical zone of the fine-grained porphyritic biotite granite; **(F)** Fluorite developed in the contact zone between the fine-grained porphyritic biotite granite and skarn; **(G)** Cu–Sn ore body developed in the garnet–diopside skarn; **(H,I)** Cu (chalcopyrite and bornite) mineralization developed in the marble zone; **(J)** W (scheelite) mineralization developed in the marble zone; **(K)** Wollastonite mineralization that is controlled by either host rock (flint-nodule limestone) or hydrothermal fluids; **(L)** Weak wollastonite alteration in the flint-nodule limestone without hydrothermal fluid. Symbols: Ccp, chalcopyrite; Fl, fluorite; Grt, garnet; Di, diopside; Sch, scheelite; Wol, wollastonite.

wollastonite is well developed in the Permian Maokou Formation (marble alteration) of the Taizibi deposit and has the potential to mineralize (Jiangxi Bureau of Geology and Mineral Resources [Jiangxi BGMR], unpublished).

Shizhushan Deposit

The Shizhushan deposit is a super-large-sized wollastonite deposit (Chen et al., 2018) in the southern part of the Mengshan complex (**Figure 2**). Currently, the Shizhushan deposit is the largest wollastonite deposit discovered worldwide (Wang et al., 2019). This deposit contains a total of 13 ore bodies and 69.55 Mt of wollastonite (Chen et al., 2018). The strata in the Shizhushan deposit include the Permian Maokou and Leping Formations and Quaternary sediments. The Maokou Formation is the most substantial ore-hosting strata and consists mainly of flint-nodule limestone and carbonaceous mudstone. Fine-grained porphyritic biotite granite intruded beneath the strata in the drill core profiles (**Figure 5D**). The fine-grained porphyritic biotite granite in the Shizhushan district was extremely altered (Chen et al., 2019), and the zircon U–Pb age has been dated at 201.4 ± 2.0 Ma (MSWD = 3.1). The EW- and NEE-trending faults crosscut the strata, granite, and ore bodies, indicating that they were post-mineralization faults (**Figures 5C,D**).

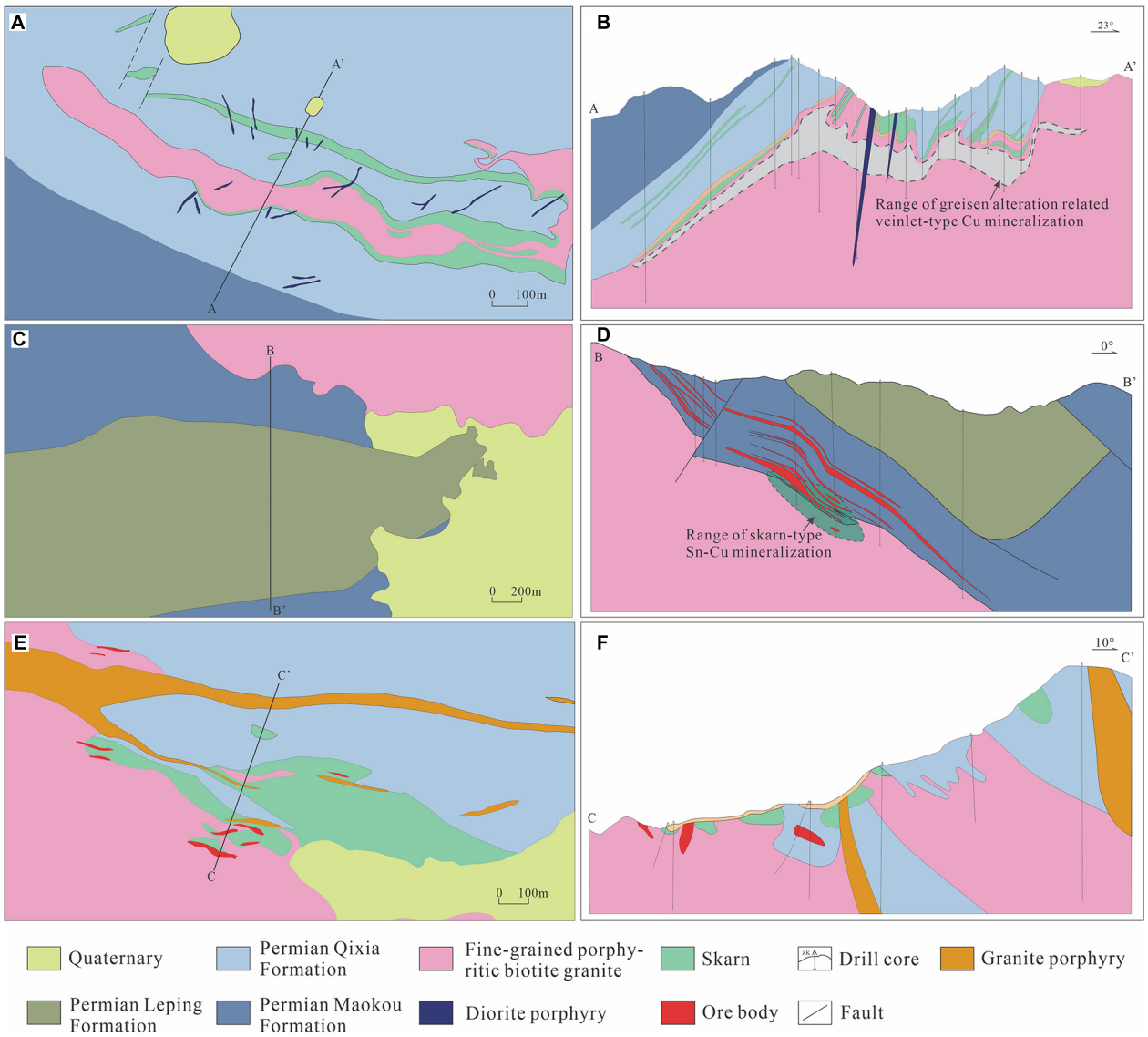

FIGURE 5 | (A,B) Simplified geological map of the Taizibi district and the geological sections of A–A' (modified after Jiangxi Bureau of Geology and Mineral Resources [Jiangxi BGMR], unpublished); **(C,D)** Simplified geological map of the Shizhushan district and the geological sections of B–B' (modified after Chen et al., 2018); **(E,F)** Simplified geological map of the Heyi district and the geological sections of C–C' (modified after Jiangxi Bureau of Geology and Mineral Resources [Jiangxi BGMR], unpublished).

The wollastonite mineralization predominantly occurs in the Permian Maokou Formation and is closely associated with marble alteration (**Figures 4K**, **5D**; Chen et al., 2018). Meanwhile, there are few Cu–Sn ore bodies (9,400 t of Cu and 5,400 t of Sn) hosted in the contact zone between the fine-grained porphyritic biotite granite and the Permian Maokou Formation (**Figure 4G**; Chen et al., 2018), which are associated with skarn alteration.

Heyi Deposit

According to the prospecting work (Jiangxi Bureau of Geology and Mineral Resources [Jiangxi BGMR], unpublished), Heyi is a small skarn-type W–Pb–Zn–fluorite deposit in the eastern part of the Mengshan complex (**Figure 2**). The four main orebodies in this district contain 700 t of WO_3, 1,100 t of Pb, 1,300 t of Zn, and 41,000 t of fluorite. The exposed strata in this district are Permian Qixia Formation (**Figures 5E,F**), which mainly comprises crystalline limestone and carbonaceous mudstone. The intrusions in the Heyi district are composed of fine-grained porphyritic biotite granite and granite porphyry. The fine-grained porphyritic biotite granite intruded as stocks and apophyses into the Permian Qixia Formation (**Figures 5E,F**), whereas the granite porphyry intruded as veins and small dikes into the fine-grained porphyritic biotite granite and the Permian Qixia Formation (**Figures 5E,F**). The primary geological structure of the Heyi district includes a series of NE- and NEE-trending folds and accompanying NE- and SE-trending fractures. The ore minerals in this district mainly include scheelite, galena, sphalerite, fluorite, chalcopyrite, and

pyrite. Skarn-type is the most important mineralization type in this district, with epidote, tremolite, and chlorite alterations being the dominant hydrothermal alteration types related to mineralization.

Alteration and Mineralization Characteristics

The above geological characteristics of the ore deposits indicated that intense hydrothermal alteration had occurred along the contact zone between the fine-grained porphyritic biotite granite and the carbonate rocks, accompanied by metal and non-metal mineralization. Based on these occurrences, the mineralization can be divided into two types: greisen-alteration-related veinlet-type and skarn-type mineralization. The detailed characteristics of these two types of alterations are described below.

The greisen-alteration-related veinlet-type mineralization mainly occurs in the apical zone of the fine-grained porphyritic biotite granite. The ore-bearing veinlets are 0.2–1 cm in width, forming 3- to 30 cm-width greisen alteration halos (**Figure 4A**). Chalcopyrite is the dominant ore mineral and occurs as medium–fine-grained anhedral crystals in the veinlets and greisen alteration halos (**Figures 4B,C**). In addition, small amounts of scheelite, sphalerite, and galena mineralization have also been reported to be related to greisen alteration (Jiangxi Bureau of Geology and Mineral Resources [Jiangxi BGMR], unpublished). Coexisting minerals in the ore-bearing veinlets primarily include quartz, muscovite, and pyrite. Based on previous studies and the observations recorded by the authors of this paper, this type of alteration is not well developed in the Mengshan district and contributes to only small amounts of metal resources.

The skarn-type mineralization occurs in the contact zone (mainly in the exo-contact zone) between the fine-grained porphyritic biotite granite and Carboniferous to Permian carbonate rocks (within a range of approximately 300 m away from the granite; **Figure 5D**). This type of alteration contributes to the super-large-scale wollastonite reserves and the majority of metal reserves in the Mengshan district. However, various types of ore minerals have been developed in different types of skarns. Sn mineralization, which mainly occurs as fine- or tiny-grained cassiterite and stannite and mainly developed in the garnet-dominated skarn (**Figures 4G**, **5D**), and the Sn content is closely related to the garnet contents in the skarns (Jiangxi Bureau of Geology and Mineral Resources [Jiangxi BGMR], unpublished). In contrast, Cu mineralization has developed not only in garnet-dominated skarn by coexisting with the Sn mineralization (**Figure 4G**) but also in the marble alteration zone by crosscutting the vein-type skarn (**Figures 4H,I**). In addition, scheelite also appears as veinlets crosscutting the marble (**Figure 4J**). Wollastonite mineralization is controlled by hydrothermal fluids and the properties of the host rocks (**Figure 4K**). If there is a widespread lack of silica in the host rocks (e.g., carbonate rocks in the Carboniferous Huanglong and Permian Qixia Formation), large-scale wollastonite mineralization is not formed (skarns in the eastern part of Mengshan district). Moreover, limited wollastonite mineralization will be formed if there is a lack of hydrothermal fluids because only a few silica in the host rocks can be activated to react with calcium (**Figure 4L**). In the Mengshan district, wollastonite mineralization mostly developed in the marble-altered flint-nodule limestone of the Permian Maokou Formation.

SAMPLING AND ANALYZING METHODS

In this study, the medium-grained porphyritic biotite granite, and its marginal phase (fine-grained porphyritic biotite granite) from the Mengshan complex, which are the most important granitic rocks leading to mineralization in this district, were sampled for the following analyses. The sample used in this study were collected from outcrops and drill core from the Mengshan district. The locations and detailed mineralogical and petrographic features of these samples are summarized in **Table 1**.

TABLE 1 | Lithology, mineralogy, and sampling site of the studied Mengshan granites.

Samples	GPS	Texture	Mineralogy
Medium-grained porphyritic biotite granite			
MS19-01	N: 28°04′34″; E: 114°55′15″	Porphyritic-like texture	30–40% phenocrysts of medium- to coarse-grained quartz (∼10%), plagioclase (∼10%), K-feldspar (15–20%), and few biotite (∼2%), and matrix of medium- to fine-grained quartz (∼20%), plagioclase (∼20%), K-feldspar (∼15%), and biotite (5–10%)
MS19-02	N: 28°04′10″; E: 114°55′08″		
MS19-03	N: 28°05′26″; E: 114°56′19″		
MS19-04	N: 28°05′54″; E: 114°56′18″		
MS19-05	N: 28°05′31″; E: 114°55′35″		
Fine-grained porphyritic biotite granite			
MS19-12	N: 28°04′47″; E: 114°57′06″	Porphyritic-like texture	20–25% phenocrysts of medium-grained quartz (∼10%) and K-feldspar (10–15%), and matrix of fine-grained quartz (∼25%), plagioclase (∼30%), K-feldspar (∼20%), and biotite (∼5%)
MS19-13	N: 28°05′12″; E: 114°56′48″		
MS19-14	N: 28°05′18″; E: 114°56′46″		
MS19-15	N: 28°03′08″; E: 114°57′24″		
MS19-16	N: 28°03′42″; E: 114°53′31″		
MS19-17	N: 28°02′27″; E: 114°55′05″		
SSZK01-123	N: 28°03′01″; E: 114°57′30″		

Zircon U–Pb Dating and Trace Element Analyses

Zircons were separated from the medium-grained porphyritic biotite granite (MS19-05) and fine-grained porphyritic biotite granite (SSZK01-123) by heavy liquid and magnetic methods followed by hand-picking at the Shougang Geological Exploration Institute. The zircons were mounted in epoxy and polished to approximately half their thickness to reveal their interiors. Examination of internal textures was performed using cathodoluminescence (CL) imaging with an Electron Microprobe at the Gaonianlinghang Company, Beijing.

The analyses were conducted using LA–ICP–MS in the Mineral and Fluid Inclusion Microanalysis Lab, Institute of Geology, Chinese Academy of Geological Sciences, Beijing. The NWR 193UC laser ablation system (Elemental Scientific Lasers, Omaha, NE, United States) was equipped with a Coherent ExciStar 200 excimer laser (Coherent, Santa Clara, CA, United States) and a Two Volume 2 ablation cell. The laser ablation system was coupled with an Agilent 7900 ICPMS (Agilent, Santa Clara, CA, United States). The detailed analytical methods have been described by Yu et al. (2019). Zircons were cleaned ultrasonically in ultrapure water and cleaned again prior to the analysis using AR grade methanol. Pre-ablation was conducted for each spot analysis using five laser shots (∼0.3 μm in depth) to remove potential surface contamination. The analysis was performed using a 30-μm diameter spot at 5 Hz with a fluence of 2 J/cm^2.

The Iolite software was used for data reduction (Paton et al., 2010). Zircon 91500 and GJ-1 were used as primary and secondary reference materials, respectively. The 91500 was analyzed twice and the GJ-1 was analyzed once every 10–12 sample analyses. Typically, 35–40 of the sample signals were acquired after 20 s of gas background measurement. The exponential function was used to calibrate the downhole fractionation (Paton et al., 2010). The measured ages of the reference materials in the batch were as follows: 91500 (1,061.5 ± 3.2 Ma, 2σ) and GJ-1 (604 ± 6 Ma, 2σ), which agreed with the reference values within definite uncertainty. The age calculations and the plotting of the concordia diagrams were performed using IsoplotR (Vermeesch, 2018).

In situ Zircon Hf Isotopic Analysis

Zircon *in situ* Hf isotope analysis was carried out using a RESOLUTION SE 193 laser-ablation system (Applied Spectra, West Sacramento, CA, United States) attached to a Thermo Fisher Scientific Neptune Plus Multicollector-Inductively Coupled Plasma Mass Spectrometer (MC–ICP–MS) (Thermo Fisher Scientific, Dreieich, Germany) at Beijing ZKKY Technology Co., Ltd. Instrumental conditions and data acquisition protocols have been described by Hou et al. (2007). The stationary spot used a beam diameter of ∼55 μm. As the carrier gas, helium was used to transport the ablated sample aerosol mixed with argon from the laser-ablation cell to the MC–ICP–MS torch by a mixing chamber. $^{176}Lu/^{175}Lu = 0.02658$ and $^{176}Yb/^{173}Yb = 0.796218$ ratios were determined to correct for the isobaric interferences of ^{176}Lu and ^{176}Yb on ^{176}Hf. For instrumental mass bias correction, Yb isotope ratios were normalized to $^{172}Yb/^{173}Yb = 1.35274$ and Hf isotope ratios to $^{179}Hf/^{177}Hf = 0.7325$ using an exponential law. The mass bias behavior of Lu was assumed to follow that of Yb; the mass bias correction protocol was described by Hou et al. (2007). Zircon international standard GJ-1 was used as the reference standard.

Whole-Rock Major and Trace Element Analyses

Whole-rock major element analyses were conducted by using x-ray fluorescence (XRF) (Primus II, Rigaku, Japan) at the Wuhan Sample Solution Analytical Technology Co., Ltd. Firstly, the sample powder (200 mesh) was placed in an oven at 105°C for drying of 12 h. Then, ∼1.0 g of the dried sample was accurately weighed and placed in the ceramic crucible, and then it was heated in a muffle furnace at 1,000°C for 2 h. After cooling to 400°C, this sample was placed in the drying vessel and weighed again in order to calculate the loss on ignition (LOI). Then, 0.6 g sample powder was mixed with 6.0 g of cosolvent ($Li_2B_4O_7$:$LiBO_2$:LiF = 9:2:1) and 0.3 g of oxidant (NH_4NO_3) in a Pt crucible, which was placed in the furnace at 1,150°C for 14 min. This melting sample was quenched with air for 1 min to produce flat disks on the fire brick for the XRF analyses.

Whole-rock trace element and rare earth element (REE) analyses were conducted using the Agilent 7700e ICP–MS (Agilent, Santa Clara, CA, United States) at the Wuhan Sample Solution Analytical Technology Co., Ltd., Wuhan, China. Firstly, 50 mg of the dried sample powder was accurately weighed and placed in a Teflon bomb. Then, 1 ml HNO_3 and 1 ml HF were slowly added into the Teflon bomb, which was put in a stainless-steel pressure jacket and heated to 190°C in an oven for >24 h. After cooling, the Teflon bomb was opened and placed on a hotplate at 140°C and evaporated to incipient dryness, and then, 1 ml HNO_3 was added and evaporated to dryness again. Then, 1 ml of HNO_3, 1 ml of MQ water, and 1 ml of internal standard solution were added into the Teflon bomb, followed by resealing and placing it in the oven at 190°C for >12 h. The final solution was transferred to a polyethylene bottle and diluted to 100 g by the addition of 2% HNO_3.

Whole-Rock Nd Isotope Analysis

Nd isotope analyses were performed on a Neptune Plus MC–ICP–MS (Thermo Fisher Scientific, Dreieich, Germany) at the Wuhan Sample Solution Analytical Technology Co., Ltd. Nine faraday collector was equipped. The faraday collector configuration of the mass system was composed of an array from L4 to H4 to monitor $^{142}Nd^+$, $^{143}Nd^+$, $^{144}Nd^+$, $^{145}Nd^+$, $^{146}Nd^+$, $^{147}Sm^+$, $^{148}Nd^+$, $^{149}Sm^+$, and $^{150}Nd^+$. The large dry interface pump and newly designed X skimmer cone and Jet sample cone were used to increase the instrumental sensitivity. An Nd single element solution from Alfa (Alfa Aesar, Karlsruhe, Germany) was used to optimize the operating parameters of the instrument. An aliquot of the international standard solution of 200-μg L-1 JNdi-1 was used regularly for evaluating the reproducibility

and accuracy of the instrument. Typically, the signal intensities of $^{144}Nd^{+}$ in JNdi-1 were >∼2.5 V. The Nd isotopic data were acquired in the static mode at low resolution. The routine data acquisition consisted often of blocks of 10 cycles (4.194 s integration time per cycle). The total time for one measurement was about 7 min.

Mass discrimination correction was carried out *via* internal normalization to a $^{146}Nd/^{144}Nd$ ratio of 0.7219 (Lin et al., 2016). The interferences of $^{144}Sm^{+}$ were corrected based on the method described by Lin et al. (2016). One JNdi-1 standard was measured for every ten samples analyzed.

RESULTS

Zircon U–Pb Ages

Zircon grains from two samples (MS19-05 of medium-grained porphyritic biotite granite and SSZK01-123 of fine-grained porphyritic biotite granite) were selected for LA–ICP–MS dating. There were some differences in the zircon morphology between the two phases of granites.

All the zircons from the medium-grained porphyritic granite were euhedral and displayed bright oscillatory zoning (**Figure 6A**), indicating a magmatic origin. The lengths of the zircons were mostly between 150 and 200 μm with length/width ratios of 2:1 to 3:1. In addition, a certain number of grains contained relict cores (**Figure 6A**).

Zircons from the fine-grained porphyritic granite were also euhedral, with the lengths and length/width ratios ranging from 100 to 200 μm and 2:1 to 4:1 (**Figure 6A**), respectively. However, the zircons from the fine-grained porphyritic granite exhibited significantly zoned core–mantle–rim textures in the CL images. The core–mantle–rim texture consisted of relict cores, bright mantles, dark mantles, and dark rims. The bright mantles displayed bright oscillatory zoning (**Figure 6A**), which was similar to the zircons from the medium-grained porphyritic granite and identical to the magmatic zircon. The dark mantles were darker than the bright mantles in CL images (**Figure 6A**) but still showed clearly oscillatory zoning texture, indicating that they were also of magmatic origin. Notably, the widths of the dark mantles were mostly between 10 and 50 μm, with only a few samples suitable for U–Pb dating and Hf isotope analysis. The rim domains had widths in the range of 5–10 μm; they showed extremely low CL emission and weak oscillatory zoning texture (**Figure 6A**) and commonly exhibited dissolution textures with a porous appearance.

The U–Pb data sets for the two samples are given in **Supplementary Table 1** and illustrated on the concordia and weighted mean plots in **Figures 6B,C**.

Medium-Grained Porphyritic Biotite Granite (MS19-05)

The zircon grains of the medium-grained porphyritic biotite granite had Th and U contents and Th/U ratios of 236–1,779 ppm, 74.8–1,198 ppm, and 0.37–0.97, respectively. Seventeen analyses of zircon grains from granite porphyry sample yielded a weighted mean $^{206}Pb/^{238}U$ age of 225.9 ± 0.5 Ma (n = 17, MSWD = 0.8; **Figure 6B**). One analysis (MS19-05-18) that was performed on the relict core of zircon yielded older age (712 Ma; **Supplementary Table 1**), which is most likely an inherited age.

Fine-Grained Porphyritic Biotite Granite (SSZK01-123)

Eighteen analyses were conducted on the zircons from the fine-grained porphyritic biotite granite for LA–ICP–MS analyses, including eleven conducted on the bright mantle domains and seven (SSZK01-123-3, 5, 7, 9, 12, 15, and 17) on the dark mantle domains. Analyses on bright and dark mantle domains had similar $^{206}Pb/^{238}U$ ages, ranging from 225.0 to 228.9 Ma and 223.2 to 230.4 Ma, respectively. The sample yielded a weighted mean $^{206}Pb/^{238}U$ age of 226.6 ± 0.5 Ma (n = 18, MSWD = 0.5; **Figure 6C**). However, the bright and dark mantle domains showed differences in the U and Th concentrations and Th/U ratios (**Supplementary Table 1**). The U and Th concentrations for the bright mantles were 257–1,683 and 76.1–1,289 ppm, respectively, with Th/U ratios ranging from 0.30 to 0.92. The dark mantles showed higher U (1,327–2,920 ppm) and Th (310–1,910 ppm) concentrations and lower Th/U ratios (0.23–0.65).

The similar ages between the medium- and fine-grained porphyritic biotite granite yielded herein demonstrated that these two intrusive phases in the Mengshan district had transitional relationships, which was consistent with the geological observations (Jiangxi Bureau of Geology and Mineral Resources [Jiangxi BGMR], unpublished).

Zircon Trace Element Compositions

The trace element compositions of the zircons from the medium- and fine-grained porphyritic biotite granite are presented in **Supplementary Table 2**. Although fractures and melt/fluid inclusions were carefully checked and avoided, one analysis spot from the medium-grained porphyritic biotite granite (MS19-05-05) exhibited apparently high light REE (LREE) abundances (**Supplementary Figure 2A** and **Supplementary Table 2**), indicating that they were affected by mineral inclusions. In addition, as suggested by Lu et al. (2016) and Lee et al. (2020), zircon trace element data with La concentrations higher than 1 ppm were assumed to have ablated mineral and melt inclusions; thus, these data were also discarded.

Overall, these zircons had similar chondrite-normalized REE patterns (**Supplementary Figures 2A,B**), characterized by moderately positive Ce anomalies (Ce_N/Ce_N^* ratios ranging from 10.12 to 1,697, mostly between 10 and 50) and strongly negative Eu anomalies (Eu_N/Eu_N^* ratios ranging from 0.04 to 0.15). Specifically, the dark mantle domain of the zircons from the fine-grained porphyritic biotite granite showed significantly lower Eu_N/Eu_N^* ratios (ranging from 0.04 to 0.09, with a mean value of 0.06) compared with zircons from the medium-grained porphyritic biotite granite (ranging from 0.06 to 0.15, with a mean value of 0.09) and the bright mantles of the zircons from the fine-grained porphyritic biotite granite (ranging from 0.05 to 0.16, with a mean value of 0.09).

The Hf contents of the zircons from the medium-grained porphyritic biotite granite ranged from 8,600 to 12,210 ppm

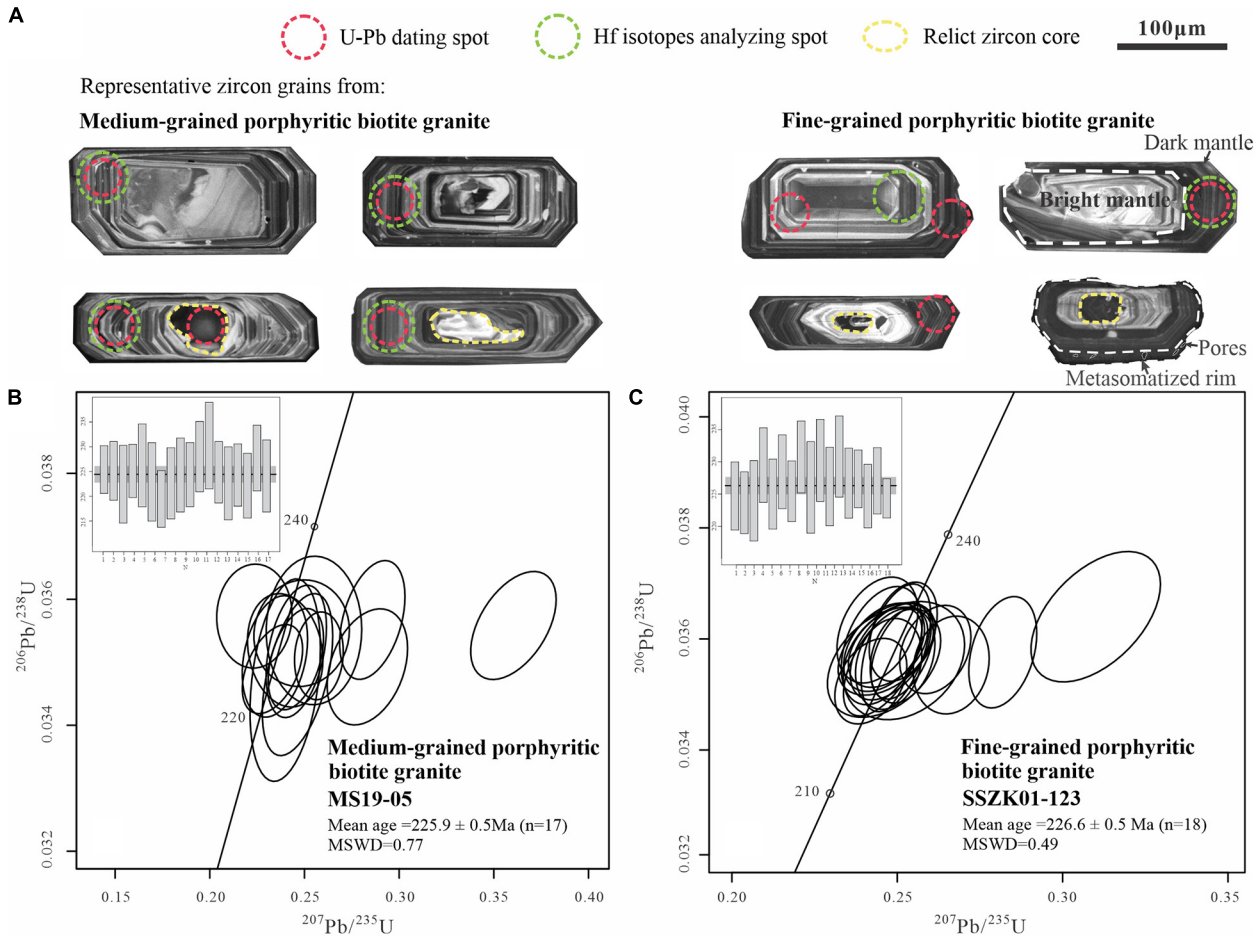

FIGURE 6 | (A) Representative cathodoluminescence (CL) images of zircons from the studied Mengshan granites; **(B,C)** U–Pb zircon concordia plots and weighted mean age of the medium-grained porphyritic biotite granite (MS19-05) and the fine-grained porphyritic biotite granite (SSZK01-123).

(mean value of 10,968 ppm), which is significantly lower than those of zircons from the fine-grained porphyritic biotite granite (10,290–12,400 ppm and 12,130–13,230 ppm for the bright and dark domains, respectively; **Figure 7A** and **Supplementary Table 2**). Moreover, Nb and Ta, substituting Zr, were relatively enriched in zircons from the fine-grained porphyritic biotite granite (mean values of 7.52 and 4.53, respectively; **Supplementary Table 2**), in contrast to the medium-grained porphyritic biotite granite (mean values of 5.73 and 2.88, respectively).

The formula proposed by Ferry and Watson (2007) allows for the calculation of the zircon crystallization temperature using the Ti content of the zircon by considering the activities of SiO_2 (αSiO_2) and TiO_2 (αTiO_2) in the host melt. The presence of quartz in the studied Mengshan granites indicates SiO_2 saturation, and αSiO_2 was set to 1.0. For the absence of titanite in the studied Mengshan granites, the αTiO_2 was set at 0.6 (Lee et al., 2017; Large et al., 2018). The results (**Supplementary Table 2**) indicated a generally decreasing temperature trend from the medium-grained porphyritic biotite granite (mean value of 755°C) to the fine-grained porphyritic biotite granite (mean value of 738°C).

Whole-Rock Major and Trace Elements

The major and trace element compositions are given in **Supplementary Table 3**, including 12 samples analyzed in this study (five samples of medium-grained porphyritic biotite granite and seven samples of fine-grained porphyritic biotite granite) and five samples from the literature (Zhong et al., 2011; the medium- and fine-grained porphyritic biotite granites were not distinguished in their study). Although the granite samples that were selected for elemental analyses in this study were collected away from the mineralization region (**Figure 2**), it was necessary to evaluate the effects of fluid alteration on the chemical compositions of the granite samples before using their data for interpretation. Firstly, it can be observed that the majority of the granite samples had LOI values of <1.5 wt%, suggesting slight effects of weathering and hydrothermal alteration on these samples. Normally, major elements such as TiO_2 and Al_2O_3 are resistant to hydrothermal alteration, whereas K_2O, Na_2O, and CaO are easily modified by alteration (Hou et al., 2013). There were weak correlations between the major elements and LOI (**Supplementary Figure 1**), indicating that the effect of hydrothermal alteration was negligible.

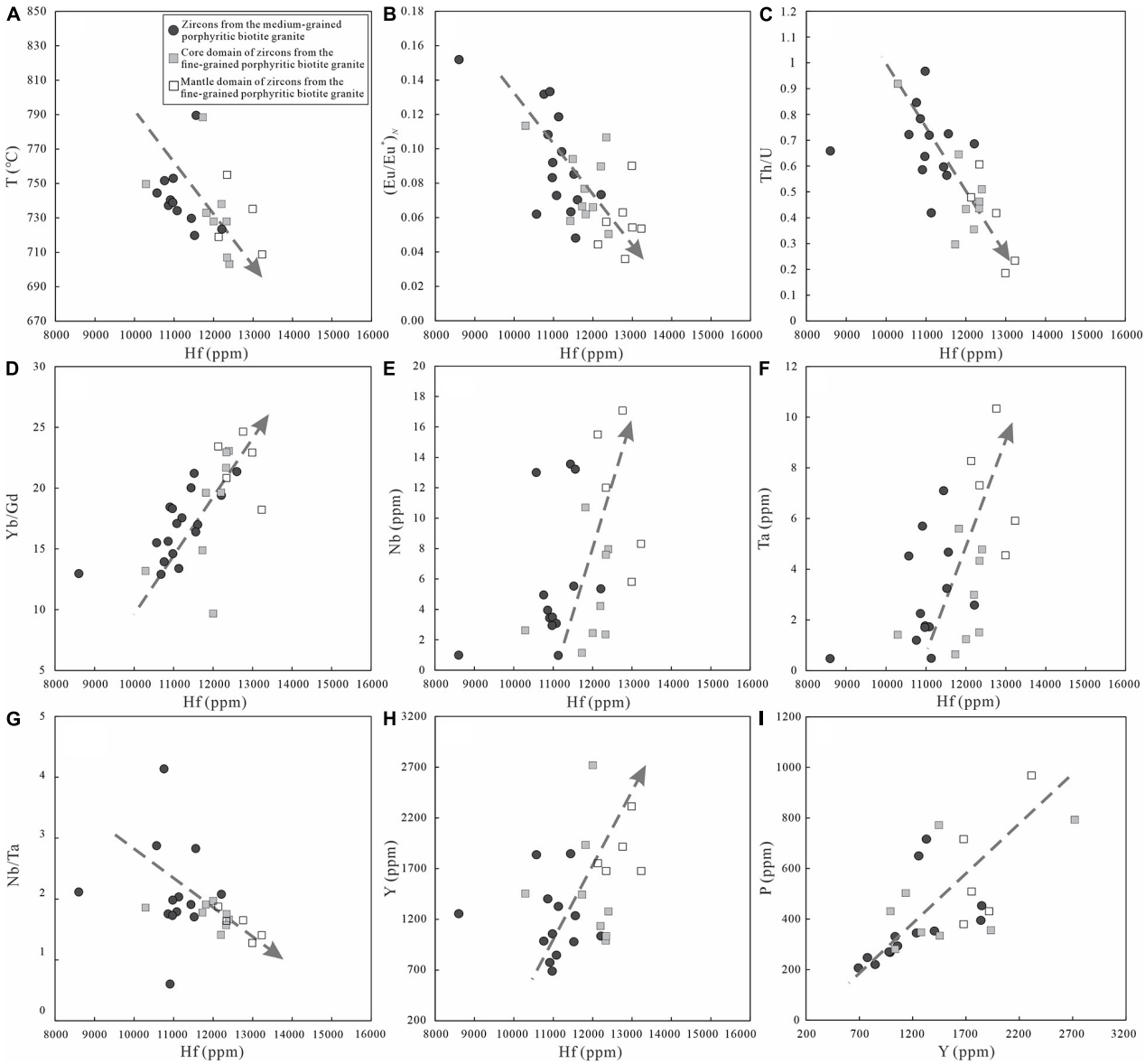

FIGURE 7 | Diagrams of **(A–H)** zircon Hf content vs. Ti-in-zircon temperature, Eu_N/Eu_N^* ratio, Th/U ratio, Yb/Gd ratio, Nb content, Ta content, Nb/Ta ratio, and Y content; **(I)** zircon Y content vs. P content.

Samples of the medium-grained porphyritic biotite granite were rich in SiO_2 (72.29–75.20 wt%) and poor in TFe_2O_3 (1.78–2.66 wt%), MgO (0.50–0.63 wt%), TiO_2 (0.24–0.40 wt%), and P_2O_5 (0.07–0.15 wt%). They all belonged to the high-K calc-alkaline series (**Figure 8A**), with K_2O contents of 4.49–5.15 wt%. Moreover, they showed weakly peraluminous feature (A/CNK = 1.02–1.07; **Figure 8B**), with Al_2O_3 contents ranging from 12.61 to 14.18 wt%. The fine-grained porphyritic biotite granite also belonged to the high-K calc-alkaline series (**Figure 8A**) and showed weakly to strongly peraluminous feature (A/CNK = 1.03–1.13; **Figure 8B**). However, the high A/CNK value of the fine-grained porphyritic biotite granite was not due to high alumina concentrations (11.30–12.39 wt%) but rather to low CaO concentrations (0.34–0.97 wt%). This can be interpreted as fractionations of calcium-bearing plagioclase, as indicated by the correlations between SiO_2 and CaO (**Figure 9C**). The fine-grained porphyritic biotite granite samples also had relatively higher SiO_2 (76.31–79.07 wt%) and lower TFe_2O_3 (0.85–1.88 wt%), MgO (0.13–0.44 wt%), TiO_2 (0.11–0.25 wt%), and P_2O_5 (0.02–0.07 wt%) contents compared with the medium-grained porphyritic biotite granite samples.

Using SiO_2 as a differentiation index for the studied granites, TiO_2, TFe_2O_3 + MgO, CaO, P_2O_5, and Zr exhibited negative correlations with the SiO_2 content, whereas Rb showed a positive correlation (**Figures 9A–F**).

The chondrite-normalized REE patterns of the studied granites are similar in overall shape (**Figure 10A**), featuring as moderately negative slope (La_N/Yb_N = 1.41–14.36) and

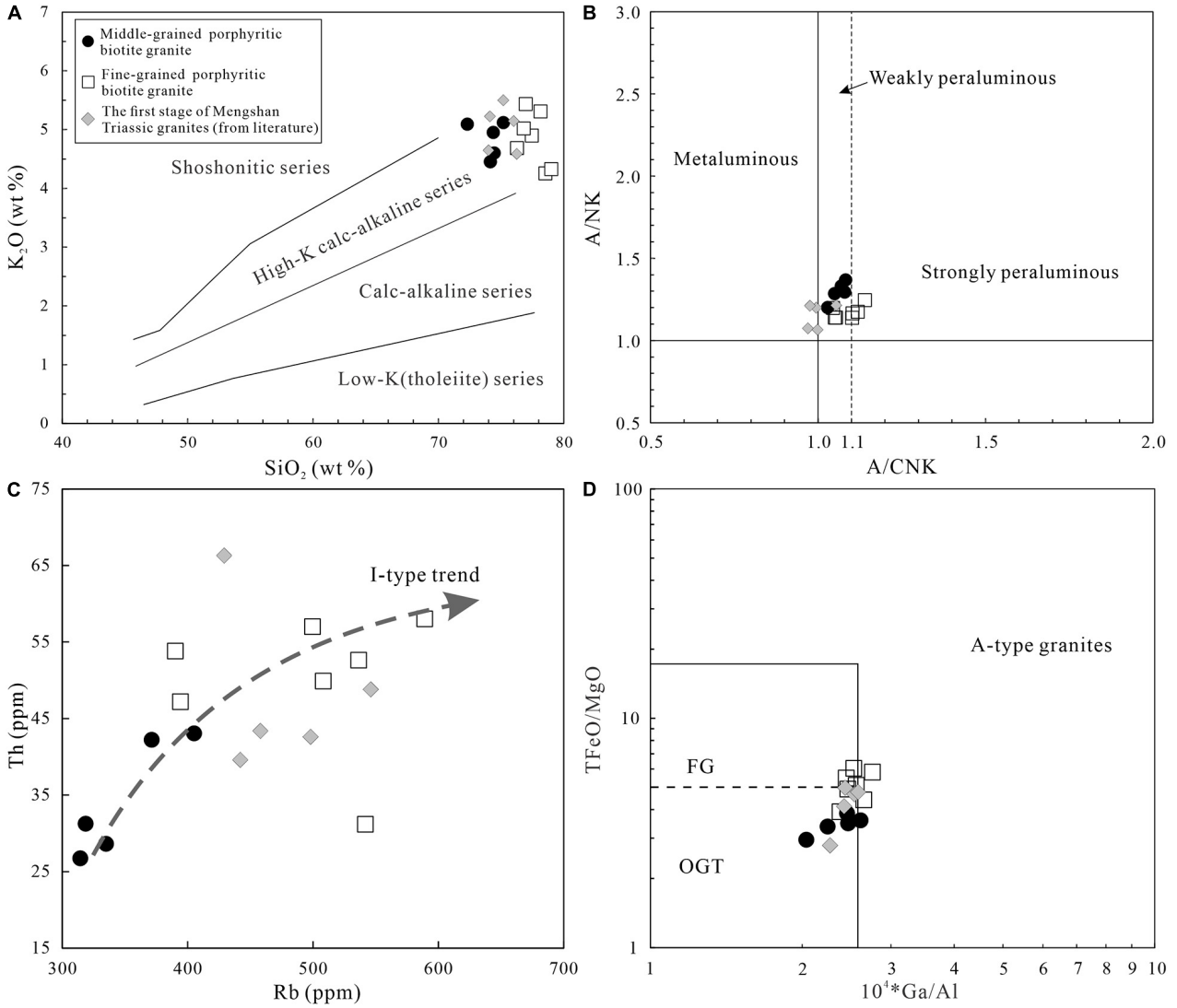

FIGURE 8 | Diagrams of **(A)** K_2O vs. SiO_2, **(B)** A/NK vs. A/CNK, **(C)** Th vs. Rb, and **(D)** TFeO/MgO vs. 10^4Ga/Al. The I-type trend was modified after Li et al. (2007). Symbols: FG, fractionated felsic granites; OGT, unfractionated I-, S-, and M-type granites.

strongly negative Eu anomalies [$(Eu/Eu^*)_N$ = 0.05–0.49]. Conversely, the fine-grained porphyritic biotite granite samples exhibited lower ΣREE (80.78–303.57 ppm) and heavy REE (HREE) (22.24–36.35 ppm) concentrations with higher La_N/Yb_N (1.41–8.01) and lower $(Eu/Eu^*)_N$ (0.05–0.15) values compared with the medium-grained porphyritic biotite granite samples [ΣREE = 142.85–297.71 ppm; HREE = 10.99–34.66 ppm; La_N/Yb_N = 8.28–14.36; $(Eu/Eu^*)_N$ = 0.24–0.49]. In the primitive-normalized trace element diagram (**Figure 10B**), the studied Mengshan granites also exhibited similar patterns; the fine-grained porphyritic biotite granite exhibited a more pronounced Ba, Sr, P, and Ti depletion and Rb, U, and Ta enrichment compared with the medium-grained porphyritic biotite granite.

Zircon Hf Isotopes

The zircon Hf isotope results for the studied Mengshan granites are presented in **Supplementary Table 4**. The majority of the spots used for U–Pb dating were also used for the *in situ* zircon Hf isotope analysis, except for six spots (SSZK01-123-03, -05, -07, -09, -12, and -15) analyzed on the dark mantle domain of the zircons from the fine-grained porphyritic biotite granite that were too narrow to conduct the Hf isotope analysis. Seventeen analyses of medium-grained porphyritic biotite granite yielded $^{176}Hf/^{177}Hf$ = 0.282700–0.282883, with ε_{Hf} (t) values ranging from 2.1 to 8.3. Twelve analyses of fine-grained porphyritic biotite granite yielded $^{176}Hf/^{177}Hf$ = 0.282717–0.282891, with ε_{Hf} (t) values ranging from 0.2 to 8.7. The corresponding Hf model ages (T_{DM}^C) of the medium- and fine-grained porphyritic biotite

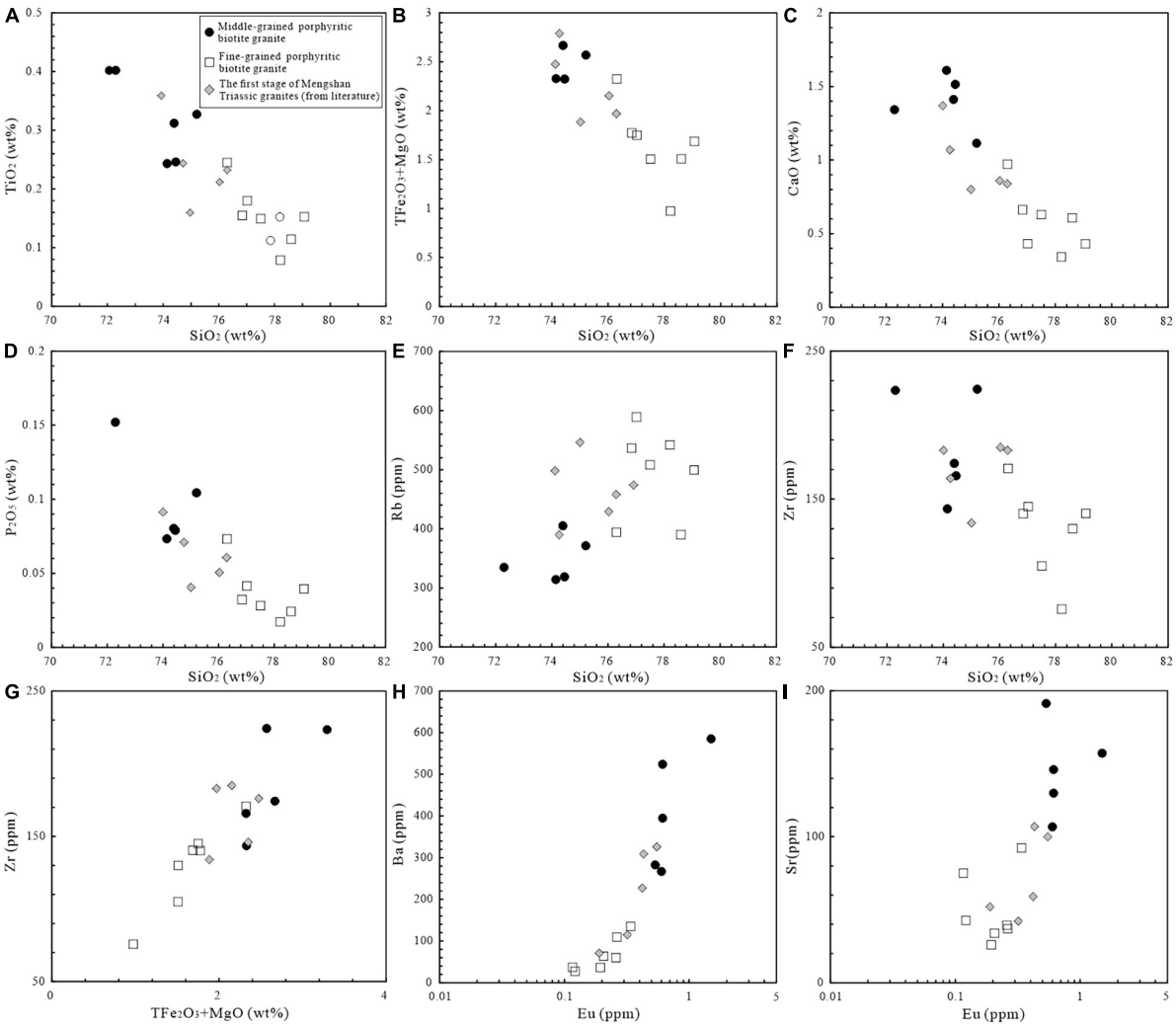

FIGURE 9 | Diagrams of **(A–F)** TiO_2, TFe_2O_3 + MgO, CaO, P_2O_5, Rb, and Zr vs. SiO_2; **(G)** Zr vs. TFe_2O_3 + MgO; **(H,I)** Ba and Sr vs. Eu for the studied Mengshan granites.

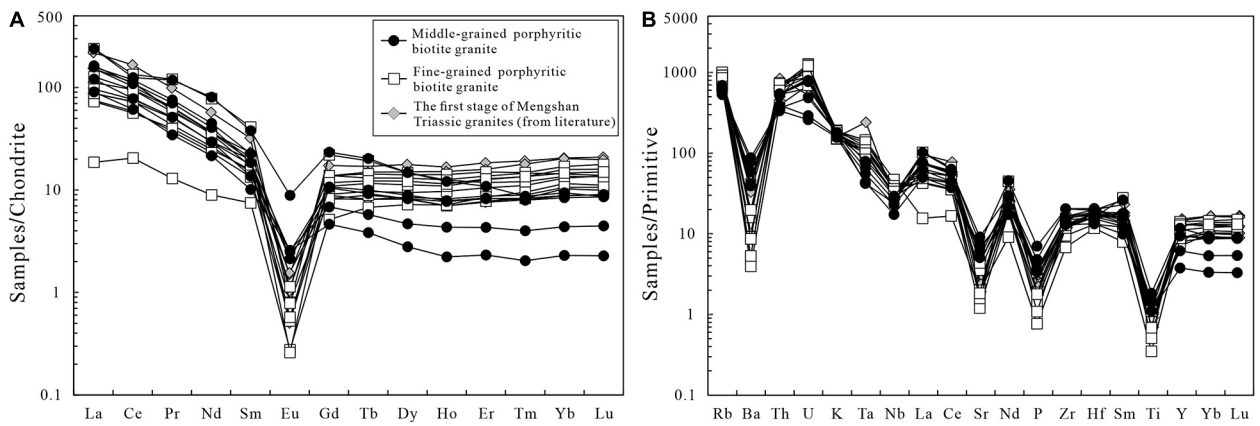

FIGURE 10 | (A) Chondrite-normalized REE patterns and **(B)** primitive-normalized trace element patterns for the studied Mengshan granites. Normalization values are from Sun and McDonough (1989).

granite ranged from 726 to 1,123 Ma and from 704 to 1,243 Ma, respectively.

Whole-Rock Nd Isotopes

The whole-rock Sm–Nd isotopic analytical results for the studied Mengshan granites are listed in **Supplementary Table 5**. The initial Nd isotopic compositions were calculated at t = 226 Ma for both the medium- and fine-grained porphyritic granite. These samples yielded $\varepsilon_{Nd}(t)$ values ranging from −7.77 to −4.09, and the corresponding two-stage Nd model ages (T_{DM2}) ranged from 1,330 to 1,630 Ma. The $\varepsilon_{Nd}(t)$ values obtained by the authors were similar to the published values, which ranged from −6.7 to −6.1 for the Mengshan Triassic granites (Zhong et al., 2011).

DISCUSSION

Triassic Granitic Magmatism in South China

Previous studies have suggested that the magmatic activity became widespread throughout the South China Block during the Triassic (ca. 260 to 200 Ma; Yu et al., 2007; Zhao et al., 2013b), which was triggered by collisional processes involving the South China Block, the North China Craton, and the Indochina Block. These Triassic magmatic rocks are characterized by peraluminous granites and minor gneissic granites, and mafic rocks are extremely rare (Wang et al., 2013). The Triassic peraluminous granites mainly include garnet-bearing granite, cordierite-bearing granite, biotite/two-mica granite, and muscovite granite (Wang et al., 2013 and references therein) and are closely associated with the mineralization of W, Sn, Nb, and Ta (e.g., Li et al., 2012; Mao et al., 2013; Feng et al., 2019).

This study compiled the published zircon U–Pb ages of the Triassic peraluminous granites and the mineralization ages (including mica Ar–Ar, molybdenite Re–Os, and scheelite Sm–Nd ages) of the Triassic ore deposits in South China (**Supplementary Table 6**). The ages of the Triassic peraluminous granites gave a wide range of 250–201 Ma (**Figure 11A**) and suggested that the Triassic magmatism in South China can be subdivided into two major magmatic episodes, namely 250–232 and 232–201 Ma, with the peak magmatic activity concentrated at around 238 and 210 Ma, respectively. Accompanied by the extensive Triassic magmatism, a series of W, Sn, Nb, Ta, Mo, and Cu deposits were exploited in South China, including the Yuntoujie W–Mo deposit with the rock-forming age of 216.8 ± 4.9 Ma (Li et al., 2012) and a mineralization age of 226.2 ± 4.1 to 216.8 ± 7.5 Ma (Li et al., 2012; Wu et al., 2012); Limu W–Sn–Nb–Ta deposit with the rock-forming age of 217.1 ± 1.4 to 212.3 ± 1.8 Ma (Li et al., 2012) and a mineralization age of 214.1 ± 1.9 to 205.2 ± 1.7 Ma (Yang et al., 2009); and Jiepai W–Cu deposit with the rock-forming age of 219.2 ± 1.5 Ma (Zhu et al., 2020) and a mineralization age of 215.5 ± 3.3 Ma (Zhu et al., 2020). Notably, the mineralization ages of the Triassic ore deposit in South China were concentrated in the range of 231–206 Ma (**Figure 11B**), synchronous with the late-episode Triassic magmatism, which is also consistent with the previous results

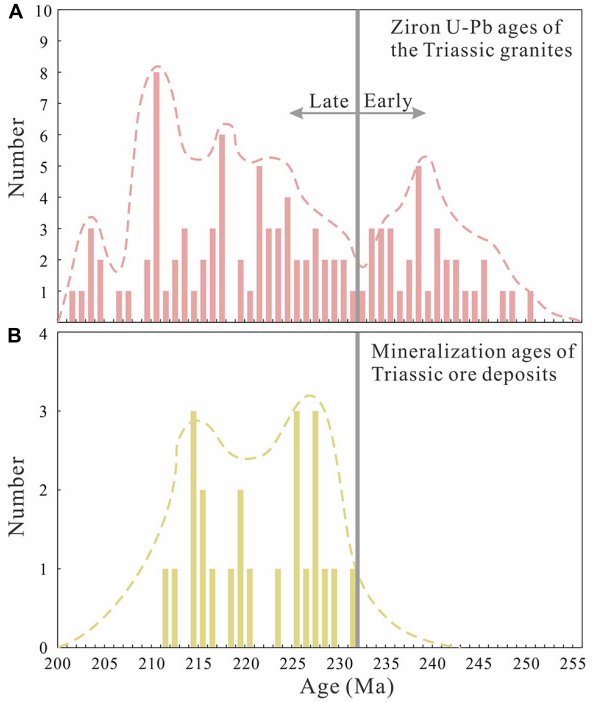

FIGURE 11 | Frequency distribution histogram of **(A)** zircon U–Pb ages of the Triassic granites in South China and **(B)** mineralization ages of the Triassic ore deposits in South China. Published U–Pb ages and mineralization ages are listed in **Supplementary Table 6**.

(230–210 Ma; Mao et al., 2013). The features mentioned above indicate that the late episode of Triassic granites in South China have more potential for the mineralization of W, Sn, Nb, Ta, Mo, and Cu. The Mengshan medium- and fine-grained porphyritic biotite granites were emplaced at similar ages of 225.9 ± 0.5 Ma and 226.6 ± 0.5 Ma (**Figure 6**), respectively, implying that these two intrusive phases were products of the late-episode Triassic magmatism in South China and also have the potential for the mineralization of W, Sn, Nb, Ta, Mo, and Cu.

Notably, the fine-grained porphyritic biotite granite in the Shizhushan deposit was dated at 201.4 Ma (Chen et al., 2019), which is different from the ages (226.6–225.9 Ma) of the first-stage granites yielded in this study, and even younger than the ages of the second- and third-stage granites in the Mengshan district (220 and 217 Ma, respectively; Zhong et al., 2011). The Shizhushan granites have not been analyzed in this study; thus, there are two possible explanations for this young age. First, there are perhaps four stages of granites in the Mengshan district, and the granite intruding in the Shizhushan district belongs to the fourth stage. Second, because the Shizhushan granites experienced extensive hydrothermal alteration (Chen et al., 2019), the U–Pb isotopic system preserved in the accessory minerals may have been modified or broken down, leading to the disturbance in the U–Pb ages (Li X. C. et al., 2021). Thus, more analytical works, e.g., detailed elemental mapping of zircon and multi-methods geochronological works, need to be conducted in the Shizhushan district.

Petrogenesis of the Mengshan Triassic Granites

Genetic Type: I-Type Affinity

All the studied Mengshan granites lacked hornblende and featured high SiO_2 contents (72.30–79.07 wt%) and Rb/Sr ratios (2.1–19.6), as well as low TFe_2O_3 + MgO (0.97–3.29 wt%), TiO_2 (0.08–0.40 wt%), and CaO (0.34–1.61 wt%) contents. These characteristics imply that the studied Mengshan granites were formed from highly evolved granitic melts. The fine-grained porphyritic biotite granite in this study exhibited relatively higher Rb contents, Cs contents, and Rb/Sr ratios and lower Sr, Eu, and Ba contents (**Figure 10B**) compared with the medium-grained porphyritic biotite granite, suggesting that the former was more evolved. Therefore, the discussion on the genetic type and magma source principally focuses on the relatively less-evolved medium-grained porphyritic biotite granite.

Unlike the S-type granite, which is strongly peraluminous (A/CNK > 1.1; Chappell and White, 1992), all the medium-grained porphyritic biotite granite in the Mengshan district showed weakly peraluminous features (A/CNK values ranging from 1.02 to 1.07; **Figure 8B**). It was inferred that the Mengshan Triassic granitoids had an I-type affinity. The P_2O_5 contents in the studied Mengshan granites were relatively low (0.07–0.15 wt%; **Supplementary Table 3**) and decreased with increasing SiO_2 contents (**Figure 9D**), which could be attributed to the fractional crystallization of apatite, because phosphorus has low solubility in metaluminous and weakly peraluminous melts (Harrison and Watson, 1984; London et al., 1999). This trend was also in agreement with the trend observed in the I-type granites in Canada (e.g., Pleasant Ridge, Mt. Pleasant, and Nashwaak; Taylor and Fallick, 1997; Zhang et al., 2020b), Australia (e.g., Lachlan Fold Belt; Chappell and White, 1992), and South China (e.g., Fogang, Nankushan, and Shirenzhang; Li et al., 2007; Jiang et al., 2018), and in contrast with the S-type granites in South China (e.g., Yashan and Dalingshang; Huang and Jiang, 2014; Li et al., 2015). Moreover, the Th content was positively correlated with the Rb content (**Figure 8C**), which is considered to be an indicator of I-type granites (Chappell and White, 1992; Li et al., 2007). The Mengshan Triassic granites also cannot be A-type because of the following evidence. First, the studied granites contained abundant hydrous minerals, e.g., biotite (**Figures 3A–D**), indicating that their parental magmas were possibly enriched in water, which contrasts with typical A-type granites containing high-temperature anhydrous pyroxene or fayalite (King et al., 1997). Second, the studied granites exhibited relatively low TFeO/MgO (ranging from 2.91 to 3.78) and low 10,000 Ga/Al (mostly lower than 2.5; **Figure 8D** and **Supplementary Table 3**) ratios, which were also distinct from the diagnostic features of A-type granites (Whalen et al., 1987; Jiang et al., 2011). Third, the studied Mengshan granites exhibited apparently lower zircon saturation temperatures (mean value of 803°C; **Supplementary Table 3**) and Ti-in-zircon temperatures (mean value of 747°C; **Supplementary Table 2**) compared with typical A-type granites (mostly higher than 820°C; Jiang et al., 2011; Zhao et al., 2013a). Consequently, the studied Mengshan granites can be assigned to highly evolved I-type granites, which is also consistent with the previous results (Zhong et al., 2011).

Magma Source and Nd–Hf Isotope Decoupling

Two petrogenetic models can be proposed to explain the formation of highly evolved I-type granites: (1) extensive fractional crystallization of mantle-derived juvenile basaltic magmas (Li et al., 2007) and (2) partial melting of metamorphic basements composed of metasedimentary and meta-igneous rocks (Chappell et al., 2012). The first model can be excluded due to the following evidence. First, if extensive fractional crystallization of mantle-derived magma took place, abundant mafic–ultramafic cumulates would be expected to occur as associates with the granitic intrusions or as syn-plutonic dikes (e.g., Gao et al., 2016), which is contrary to the observations recorded by the authors (**Figure 2**). Second, if magmatic underplating occurred, as in Northeast China (Jahn et al., 2001; Wu et al., 2011), large-scale syn-granitoids and associated mantle-derived mafic-ultramafic magmas would be emplaced in the western Jiangxi Province. However, the Triassic mafic-ultramafic igneous rocks are very rare in South China, with only Daoxian gabbro xenoliths (zircon U–Pb ages of 224 Ma; Guo et al., 1997) observed in the Cretaceous basalt in southern Hunan Province. Third, Wang and Pupin (1992) argued that in the zircons of mantle-derived granites, Hf is negatively correlated with Y, and there is a significant negative correlation between Y and P. In contrast, for crust-derived granite, these elements are inversely correlated. The substantial positive correlations between zircon Hf and Y and between Y and P (**Figures 7H,I**) in the studied Mengshan granite indicated that the granites were generated from the crust instead of the mantle. Fourth, the studied granites had $\varepsilon_{Nd}(t)$ values ranging from –7.77 to –4.09 (**Supplementary Table 5**), with the corresponding two-stage Nd model ages (T_{DM2}) ranging from 1,630 to 1,330 Ma, indicating that they were mainly derived from partial melting of the Mesoproterozoic metamorphic basement. The Nd isotopic compositions of the Proterozoic crusts in South China have been well defined in previous studies (Chen and Jahn, 1998). Notably, the majority of the Nd isotopic data of the studied Mengshan granites were in the evolution envelope of the Mesoproterozoic metamorphic basements in South China (**Figure 12A**), with a few samples plotted into the Neoproterozoic juvenile crust. Consequently, the Proterozoic metamorphic basements composed of metasedimentary and meta-igneous rocks could be a favorable scenario for the studied Mengshan I-type granites.

The whole-rock CaO/Na_2O ratio was found to be effective in distinguishing granite source compositions (Sylvester and Liegeois, 1998). The studied Mengshan granites had relatively high CaO/Na_2O (0.39–0.51; **Supplementary Table 3**), indicating that they were derived from plagioclase-rich and clay-poor sources. Meanwhile, the studied granites also exhibited low Al_2O_3/TiO_2 ratios (38.5–57.3), with all the samples plotted along a mixing line between the pelite- and basalt-derived melts (**Figure 12B**), which was similar to the Triassic I-type granitoids and different from the Triassic S-type granitoids in Hunan Province (Wang et al., 2007), indicating a binary mixed source (Chappell and White, 1992; Jung et al., 2000). It is worth comparing the major element compositions of the studied Mengshan granites with the compositions of the

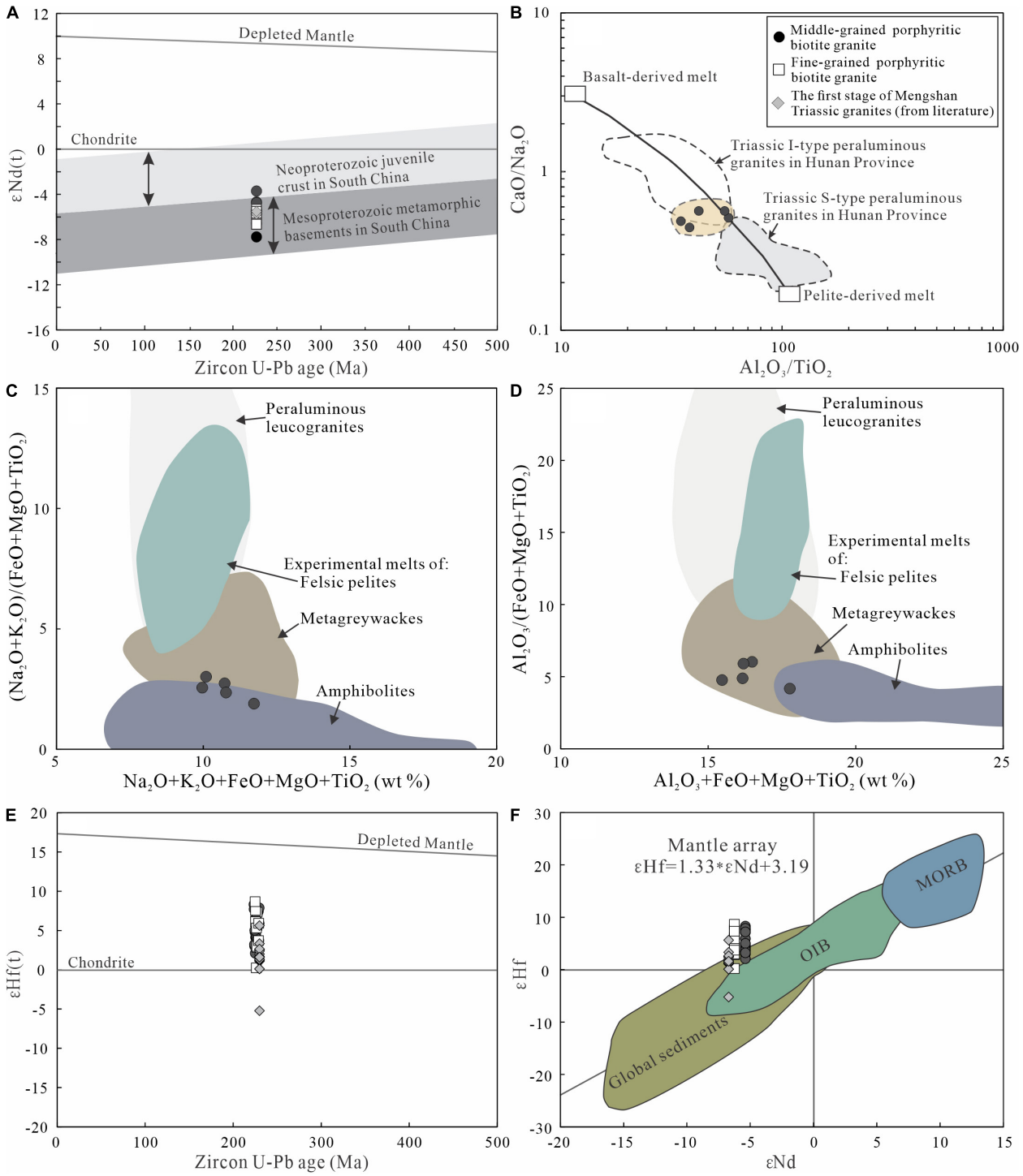

FIGURE 12 | (A) Diagram of CaO/Na_2O vs. Al_2O_3/TiO_2, the fields of Triassic I- and S-type peraluminous granites in Hunan Province, and the mixing curve between the basalt- and pelite-derived melts are from Wang et al. (2007) and references therein; **(B)** Diagram of whole-rock εNd(*t*) vs. zircon U–Pb ages; the fields of the Neoproterozoic juvenile crust and the Mesoproterozoic metamorphic basement in South China are from Chen and Jahn (1998) and Mao et al. (2017); **(C,D)** Compositional fields of experimental melts derived from the melting of felsic pelites, metagreywackes, and amphibolites (Patiño Douce, 1999); **(E)** Diagram of zircon εHf(*t*) vs. zircon U–Pb ages; **(F)** Whole-rock εNd vs. zircon εHf diagram for the Mengshan granites; the fields for mid-ocean ridge basalt (MORB), ocean island basalt (OIB), and Global sediments are from Vervoort and Blichert-Toft (1999).

experimental granitic liquids that were melted from felsic pelites, metagreywackes, and amphibolites (Patiño Douce, 1999) to help resolve possible protoliths. In **Figures 12C,D**, the data for the studied Mengshan granites appear to fall within the range of metagreywackes and amphibolites, implying that the I-type Mengshan granites could be derived from the partial melting of a mixed source composed of metagreywackes and amphibolites.

Notably, relatively depleted and heterogeneous zircon Hf isotopic compositions (epsilon Hf values ranging from 2.1 to 8.3 and from 0.2 to 8.7, respectively; **Figure 12E**), as well as significant decoupling of the Nd and Hf isotopic systems were found in the studied Mengshan granites (**Figure 12F**). Similar zircon Hf isotopic features have also been reported in the second and third stages of the Triassic granites in the Mengshan district (Zhong et al., 2011). Zhong et al. (2011) suggested that the decoupling of Nd and Hf isotopic systems in the Mengshan granites implied that these granites were generated from the partial melting of Neoproterozoic arc-related magmas that were related to the metasomatized mantle wedge. In fact, the decoupling of the Nd and Hf isotopic system has been widely observed in magmatic rocks, for instance, in the magmatic rocks from the North Qilian Orogen (Huang et al., 2019), the Chinese Altai Orogen (Zhang et al., 2019), and the Jiuling batholith (Tang et al., 2014; Wang et al., 2018). These studies proposed two possible explanations for the decoupling of the Nd–Hf isotopic systems, including magma mixing and the disequilibrium melting process (Tang et al., 2014; Huang et al., 2019; Zhang et al., 2019). Magma mixing can be ruled out due to the lack of clear field evidence in the Mengshan district, e.g., the coeval mafic rocks in this district and the mafic microgranular enclaves that were proved to be derived from mafic magmas. We suggested that the disequilibrium melting process might result in the decoupling of the Nd and Hf isotopic systems for the studied Mengshan granites because of the following reasons. First, inherited/relict zircons were common in the studied Mengshan granites (**Figure 6A**; Zhong et al., 2011), suggesting that the magma source had a relatively high Zr concentration (>100 ppm; Tang et al., 2014), the melting was relatively rapid, or the melting temperature was relatively low. It was mentioned above that the studied Mengshan granites had relatively low zircon saturation temperatures (mean value of 803°C; **Supplementary Table 3**) and Ti-in-zircon temperatures (mean value of 759°C; **Supplementary Table 2**). Thus, a significant amount of ^{177}Hf could be retained at the source due to the residual zircons in the magma source (Tang et al., 2014; Wang et al., 2018), leading to elevated ^{176}Hf/^{177}Hf ratios and the decoupled Nd–Hf isotopic system. In this case, zircon Hf isotopic compositions may not reflect the isotopic composition of the magma source, whereas the whole-rock Nd isotopic composition probably reflects the isotopic composition of the magma source (Tang et al., 2014; Zhang et al., 2019). Second, there were large variations in the zircon $\varepsilon_{Hf}(t)$ values for the studied Mengshan granites (>8 epsilon units in this study, and even >10 epsilon in Zhong et al., 2011). Commonly, the Hf isotopic heterogeneity recorded in the zircons may be explained by magma mixing of multiple sources (e.g., Boss, 2008; Couzinié et al., 2016); however, there is a lack of clear field evidence for magma mixing in the Mengshan district. By investigating the isotopic compositions of the Neoproterozoic Jiuling Batholith, Tang et al. (2014) and Wang et al. (2018) determined that the abnormally high zircon Hf isotopes (relative to whole-rock Nd and Hf isotopes) and large isotopic variations in the granitic rocks could result from disequilibrium melting of zircon-bearing crustal rocks. Therefore, we suggested that the relatively depleted and heterogeneous zircon Hf isotopic composition, as well as significant decoupling of the Nd–Hf isotopic system in the studied Mengshan granites resulted from disequilibrium melting, and the zircon Hf isotopic composition could not represent the isotopic composition of the magma source.

In conclusion, the studied Mengshan Triassic granites were likely derived from the disequilibrium melting of Proterozoic metamorphic basements that were composed of meta-igneous and metasediments.

Evolutionary Process

Zircon chemistry as an indicator of magmatic evolution and melt–fluid interaction

Zircons from the medium-grained porphyritic biotite granite and the bright and dark mantle domains of zircons from the fine-grained porphyritic biotite granite exhibited clear oscillatory zoning in the CL images (**Figure 6A**), extremely low LREE contents, and significantly positive Ce anomalies (**Supplementary Figures 2A,B**), which are similar to the characteristics of magmatic zircon (Yang et al., 2013; Li et al., 2018). Meanwhile, in the zircon discrimination diagrams proposed by Hoskin (2005), all the zircons from the studied Mengshan granites were plotted in the magmatic region (**Supplementary Figures 2C,D**). Based on these criteria, it can be inferred that the analyzed zircon grains from the studied Mengshan granites are all magmatic zircons.

Although zircon is acknowledged to be one of the early crystallized phases in granites, highly evolved granites have been reported to crystallize zircons at a late stage (e.g., Li et al., 2014; Jiang et al., 2019). In zircon, Th, U, Y, and Hf contents, and Th/U, Yb/Gd, and $(Eu/Eu^*)_N$ ratios are largely controlled by the magmatic evolution (e.g., Wooden et al., 2006; Li et al., 2014; Lee et al., 2017; Large et al., 2018); thus, the variations of these trace elements can be used to track the magmatic evolution. Experiments have revealed that the fractional crystallization of metaluminous and peraluminous granitic melts increases the Hf content in zircon (Linnen and Keppler, 2002), leading to the occurrence of Hf-enriched zircons (even hafnon; Yin et al., 2013) in highly evolved granites. For the Mengshan granites, the Hf contents in the zircons from the fine-grained porphyritic biotite granite (mean values of 12,753 and 11,802 ppm for the dark and bright mantle domains, respectively) were significantly higher than those in the zircons from the medium-grained porphyritic biotite granite (mean value of 11,068 ppm; **Figure 7** and **Supplementary Table 2**), suggesting that the fine-grained porphyritic biotite granite was more evolved. The Ti-in-zircon temperature correlated with the zircon Hf contents (**Figure 7A**) and roughly decreased from the medium-grained porphyritic biotite granite (mean value of 755°C) to the fine-grained porphyritic biotite granite (mean values of 744 and 734°C for the bright and dark mantle domains,

respectively), which is also consistent with the evolutionary trend. Based on previous research (Belousova et al., 2002; Jiang et al., 2019), owing to the enrichment of U and Th or increased partition coefficient for Th and U between zircon and magmatic melts, the zircon with high U and Th and low Th/U ratios will crystallize from more evolved granitic melts. The increases in zircon Yb/Gd of the Mengshan granites could have resulted from apatite fractionation, with preferential removal of middle REE (Sm and Gd) from the melt compared to LREE and HREE (Lee et al., 2017). Fractional crystallization of plagioclase also would decrease the $(Eu/Eu^*)_N$ ratios in zircon (e.g., Lee et al., 2017; Duan et al., 2019; Zhang et al., 2020a). Furthermore, the Nb/Ta ratios in zircon were largely controlled by their contents in the magmatic melts (e.g., Jiang et al., 2019); thus, the Nb/Ta ratio in both magmatic melts and zircons would decrease with magmatic evolution due to the fractionation of biotite (Stepanov et al., 2014). The zircons from the studied Mengshan granites exhibited noticeable trends in which the Hf content was negatively correlated with the $(Eu/Eu^*)_N$, Th/U, and Nb/Ta ratios (**Figures 7B,C,G**) but positively correlated with the Yb/Gd ratio (**Figure 7D**). Moreover, the dark mantle domains of the zircons from the fine-grained porphyritic biotite granite yielded the lowest $(Eu/Eu^*)_N$ (mean value of 0.06), Th/U (mean value of 0.38), and Nb/Ta (mean value of 1.57) ratios, and the highest Yb/Gd ratio (mean value of 22.02). Together, these results indicated that the fine-grained porphyritic biotite granite crystallized from more evolved melts, with plagioclase, apatite, and biotite being fractionated during the magmatic evolution.

In particular, the rim domains of the zircons from the fine-grained porphyritic biotite granite were porous and showed extremely low CL emission and weak oscillatory zoning texture (**Figure 6A**), which were similar to the morphology of hydrothermal-origin zircons from highly evolved granites (e.g., Pettke et al., 2005; Li et al., 2014). Geisler et al. (2007) suggested that the occurrence of porous zircons could be attributed to the dissolution–reprecipitation process between zircon grains and aqueous fluids, which involves the thermodynamics of solid solution–aqueous solution systems. This point of view can be further confirmed by the chemical compositions of the porous zircons from the highly evolved granites, which commonly contain relatively lower ZrO_2 and SiO_2 contents; higher HfO_2, CaO, Al_2O_3, U, Th, P_2O_5, common Pb, Sn, and light REE contents; and more pronounced Eu anomalies (e.g., Pettke et al., 2005; Li et al., 2014; Wang and Ren, 2018). Although the rim domains of zircons in the studied granites were too narrow (5–10 μm) to conduct the LA–ICP–MS analyses, their morphological features suggested that they were formed by fluid metasomatism and thus implied the occurrence of melt–fluid interactions in the fine-grained porphyritic biotite granite.

Whole-rock geochemistry as an indicator of magmatic evolution and melt–fluid interaction

The CaO content decreased with increasing SiO_2 from the medium-grained porphyritic biotite granite to fine-grained porphyritic biotite granite (**Figure 9C**), indicating that the fractionation of plagioclase occurred during the magmatic evolution, which is supported by notable depletion in the Sr, Ba, and Eu anomalies (Nash and Crecraft, 1985; Bea et al., 1994; **Figure 10B**). In addition, the negative correlations of Ba and Sr vs. Eu were indicative of varying degrees of plagioclase and K-feldspar fractionations (**Figures 9H,I**). The decrease of P_2O_5 from the medium-grained porphyritic biotite granite to fine-grained porphyritic biotite granite (**Figure 9D**) indicated the fractionation of apatite (Harrison and Watson, 1984; London et al., 1999). The decreases in TFe_2O_3 + MgO and TiO_2 with increasing SiO_2 contents from the medium-grained porphyritic biotite granite to fine-grained porphyritic biotite granite (**Figures 9A,B**) indicated the fractionations of ferromagnesian minerals and Ti-rich phase, including biotite and Fe-Ti oxide. Zircon crystallization consumes major Zr in peraluminous magmas (Watson and Harrison, 1983; Dostal and Chatterjee, 2000); thus, a decrease in Zr concentrations from the medium-grained porphyritic biotite granite to fine-grained porphyritic biotite granite (**Figure 9F**) resulted from the fractionation of zircon. Moreover, the positive correlation between TFe_2O_3 + MgO and Zr (**Figure 9G**) also suggests the co-fractionation of biotite and zircon.

However, a series of studies have indicated that unusually low K/Rb (<150), Nb/Ta (<6), and Zr/Hf (<26) ratios in evolved granites can be attributed to melt–fluid interactions (Shaw, 1968; Dostal and Chatterjee, 2000; Jiang and Zhu, 2017). All the studied Mengshan granites had K/Rb ratios lower than 150 (**Supplementary Table 3**), with the K/Rb ratios in the fine-grained porphyritic biotite granite ranging from 72.39 to 91.12. The Nb/Ta ratios of the studied Mengshan granites were generally less than 6, with the lowest ratio down to 2.02 (**Figure 13A**). Moreover, the fine-grained porphyritic biotite granite demonstrated relatively low Zr/Hf ratios (mean value of 26.86, with the lowest ratio of 21.26). The fine-grained porphyritic biotite granite also displayed positive correlations in the diagrams of Nb/Ta vs. K/Rb and Zr/Hf (**Figures 13A,B**). These results suggested that the melt–fluid interaction occurred during the formation of fine-grained porphyritic biotite granite.

Redox State of Mengshan Triassic Granites

Whole-Rock Fe_2O_3/FeO Ratio

The whole-rock Fe_2O_3/FeO ratio is an empirical redox indicator (e.g., Blevin, 2004; Wang et al., 2014). However, this parameter can be easily affected by hydrothermal alterations or surficial weathering. Meanwhile, for granitic rocks with high SiO_2 contents (>72 wt%) and low total FeO (<2 wt%), the Fe_2O_3/FeO ratios commonly yield unrealistic values in terms of the magmatic fO_2 values, and other methods of determining redox state need to be used (Blevin, 2004). Thus, the whole-rock Fe_2O_3/FeO ratios were used in this study for reference only.

The whole-rock Fe_2O_3/FeO ratios for the studied Mengshan granites ranged from 0.11 to 1.59 (mean value of 0.47; **Supplementary Table 3**). Among these samples, only one sample of medium-grained porphyritic biotite granite (MS19-05) exhibited relatively high TFeO values (>2 wt%) and plotted close

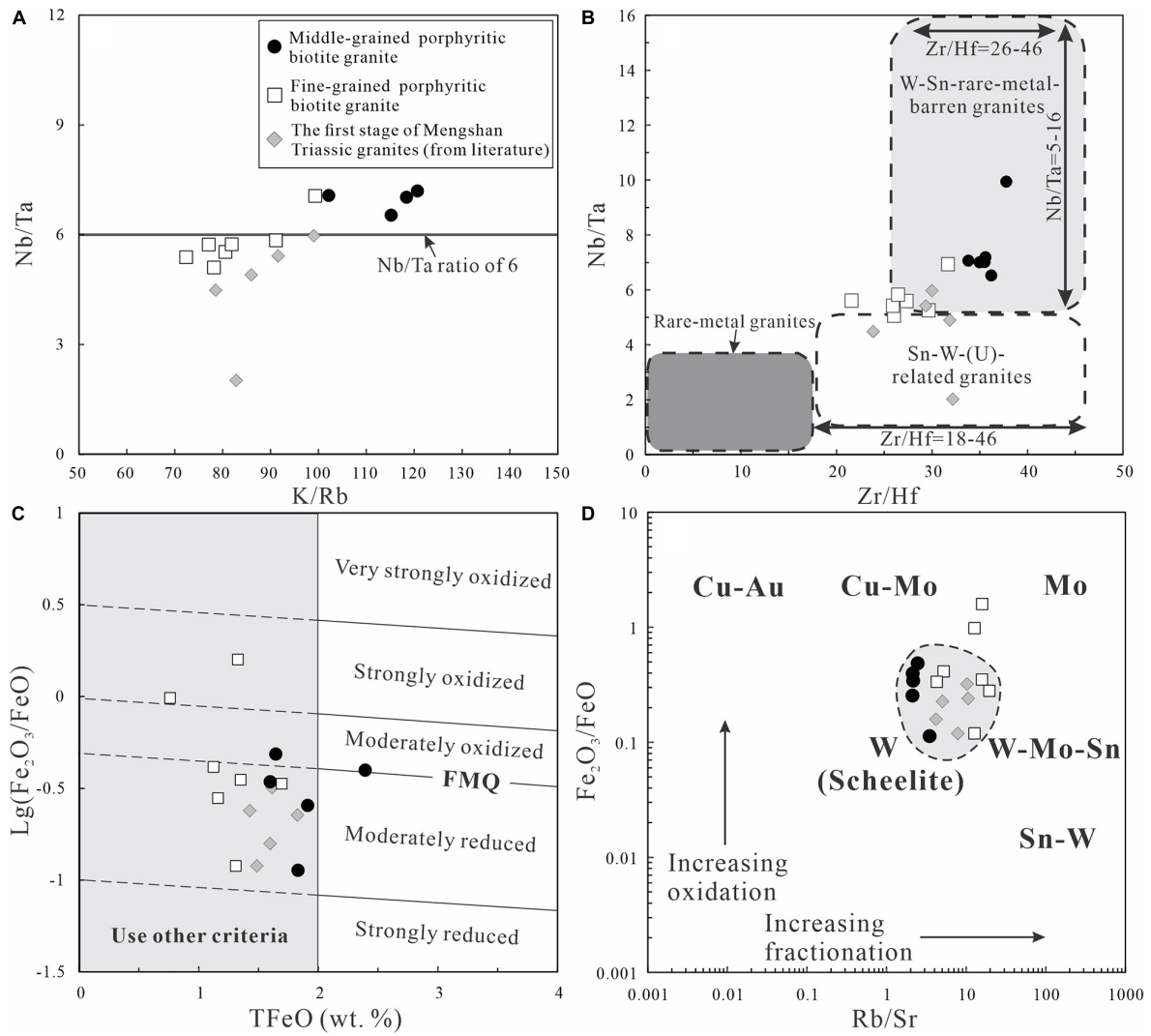

FIGURE 13 | Diagrams of **(A,B)** Nb/Ta vs. K/Rb and Zr/Hf; **(C)** lg (Fe_2O_3/FeO) vs. TFeO (modified after Blevin, 2004); and **(D)** Fe_2O_3/FeO vs. Rb/Sr (modified after Černý et al., 2005). The fields of barren granite, Sn–W–(U) granites, and rare-metal granites in **(B)** are from Ballouard et al. (2016). "Use other criteria" in **(C)** means that for granitic rocks that have low total FeO (<2 wt.%) contents, the Fe_2O_3/FeO ratios commonly yield unrealistic values in terms of the magmatic fO_2 values, and other methods of determining redox state need to be used (Blevin, 2004).

to the boundary between "moderately reduced" and "moderately oxidized," which is close to the fayalite-magnetite-quartz (FMQ) buffer (**Figure 13C**; Blevin, 2004). Although other samples had low TFeO values, the relatively low Fe_2O_3/FeO ratios (mostly lower than 0.5) indicated a moderately reduced redox state for the studied Mengshan granites.

Zircon Oxygen Barometer

Owing to the substitution of Ce^{4+} and Eu^{3+} with Zr^{4+} in magmatic zircon, Ce and Eu anomalies in zircon can reflect the redox states of magmatic melts (Ballard et al., 2002; Lu et al., 2016; Shu et al., 2019). Ce anomalies are normally reflected by Ce_N/Ce_N^* [where $Ce_N/Ce_N^* = Ce_N/(La_N^*Pr_N)^{0.5}$] and Ce^{4+}/Ce^{3+} ratios. However, La and Pr concentrations in magmatic zircons are commonly too low, even lower than the detection limit (Trail et al., 2012), leading to the rare use of the Ce_N/Ce_N^* ratio. The Ce^{4+}/Ce^{3+} ratio in zircon can be calculated following the method proposed by Ballard et al. (2002) based on mineral–melt partitioning of trace elements using a lattice-strain model (Blundy and Wood, 1994). Eu anomalies can be reflected by the Eu_N/Eu_N^* ratio [where $Eu_N/Eu_N^* = Eu_N/(Sm_N^*Gd_N)^{0.5}$]. Accordingly, more pronounced Ce positive anomalies (higher Ce^{4+}/Ce^{3+}) and weaker Eu negative anomalies (high Eu_N/Eu_N^*) indicate an oxidized redox state and *vice versa*. It is noteworthy that fractional crystallization of plagioclase is well known to deplete Eu in melts and zircons (Deering et al., 2016). Recently, by using a Monte Carlo simulation, Nathwani et al. (2021) also proposed that any redox effects on the zircon Eu_N/Eu_N^* ratio are subordinate compared with changes in the melt composition controlled by fractional crystallization. As mentioned above,

in the studied Mengshan granites, the zircon Eu_N/Eu_N^* ratios were largely controlled by the magmatic evolution, as evidenced by the significantly negative correlation between the zircon Eu_N/Eu_N^* ratios and Hf contents (**Figure 7B**), indicating that the zircon Eu_N/Eu_N^* ratio of the studied Mengshan granites should not be used to evaluate the magmatic redox state. In this study, the Geo-fO_2 software (Li et al., 2019) was used to calculate the Ce^{4+}/Ce^{3+} ratios. The quantitative oxygen fugacity (fO_2) was calculated based on two methods proposed by Trail et al. (2011) and Loucks et al. (2020), respectively. The former one is a widely used method that determines the oxygen fugacity based on the zircon Ce anomaly, crystallization temperature, pressure, and parental melt composition, whereas the latter one is mainly based on the ratios of Ce, U, and Ti contents in zircon.

Zircons from the medium- and fine-grained porphyritic biotite granite yielded a decreasing trend of Ce^{4+}/Ce^{3+} ratios from 4.12 to 166.78 (median value of 50.0) and 2.81 to 88.91 (median value of 23.3) (**Supplementary Table 2**), implying that the studied Mengshan granites had a relatively reduced redox state, and the fine-grained porphyritic biotite granites were more reduced. The absence of correlation between zircon Ce^{4+}/Ce^{3+} and Eu_N/Eu_N^* in the studied Mengshan granites (**Figure 14A**) also suggested that the zircon Eu_N/Eu_N^* ratios cannot be used to reflect the magmatic redox state.

For the zircons from the medium- and fine-grained porphyritic biotite granite, the ΔFMQ values (ΔFMQ^1) were calculated based on the method proposed by Trail et al. (2011), which yielded a very wide range of −4.1 to +6.5 and −7.1 to +4.4, respectively (**Supplementary Table 2**). Previous studies have found that it is difficult to precisely estimate the oxygen fugacity by using this method because there are superposed uncertainties in calculating the $(Ce/Ce^*)_D$ and estimating the zircon crystallization temperature and melt water content (Shu et al., 2019), leading to unrealistic ΔFMQ values (out of the range of terrestrial magmas, which range from −3 to +6; Carmichael and Ghiorso, 1990). Thus, the varied ΔFMQ^1 values (>10 units) in the studied Mengshan granites indicated that the calculation method proposed by Trail et al. (2011) was not suitable in this study. Differently, the ΔFMQ^2 values (calculated based on the methods proposed by Loucks et al., 2020) in the Mengshan granites were more credible and varied from −1.9 to +1.4 (median = + 0.9; **Supplementary Table 2**) and −3.0 to +1.0 (median = −0.4), respectively. In the diagram of $\log fO_2$ vs. T (Ti-in-zircon temperature), most samples plotted around the nickel–nickel oxide (NNO) buffer (**Figure 14B**). This result was consistent with the low zircon Ce^{4+}/Ce^{3+} ratios (mostly lower than 90; **Supplementary Table 2**), indicating that the studied Mengshan granites had a relatively reduced redox state.

Notably, both the zircon Ce^{4+}/Ce^{3+} ratios and ΔFMQ values decreased with the magmatic evolution from the medium- to fine-grained porphyritic biotite granite. As previously summarized, three factors were proposed to be the dominant factors in lowering the oxygen fugacity of the magma, namely the assimilation of reduced wall rocks, fractionations of magnetite and hematite, and degassing of oxidized volatiles (Sun et al., 2015). The effects of the wall-rock assimilation can be excluded, as they were not recorded by the whole-rock geochemistry and Nd isotopes or zircon composition. The second factor can also be ruled out because magnetite is rare in the studied Mengshan granites. Thus, magmatic volatile degassing is the only possible mechanism that can explain the relatively lower oxygen fugacity in the fine-grained porphyritic biotite granite. The variations in oxygen fugacity in the studied Mengshan granites were similar to those in the Zhuxi W–Cu deposit in South China (Zhang et al., 2020a). In the Zhuxi deposit, with the magmatic evolution, the oxygen fugacity gradually decreased from the biotite granite and muscovite granite to the granite porphyry, which was thought to be related to the multistage magma degassing (Zhang et al., 2020a). This degassing process may occur during the initial stages of cooling when the magmatic system is open or at a later stage when the accumulated volatile pressure at the top of the magma chamber overcomes the tensile strength of the solidified crystallization shell and the confining pressure (Burnham, 1979).

Mineralization Potential of the Mengshan Triassic Granites

Until now, mineral explorations in the Mengshan district have mainly focused on non-metal resources (You et al., 2006; Chen et al., 2018), e.g., wollastonite, marble, and diopside, whereas the exploration of metal-related ore deposits/occurrences is rare. The abovementioned works of research on the field geology, geochronology, petrochemistry, and magmatic redox state in this study indicated that the Mengshan Triassic granites have the potential for metal mineralization due to the following factors.

(1) Triassic granitic magmatism is widespread in South China (**Figure 1**). By compiling the zircon U–Pb ages, these granites were mainly emplaced at 250–201 Ma and could be divided into two episodes, namely 250–232 Ma and 232–201 Ma. The early episode (250–232 Ma) granites were deemed to have formed under relatively compressional stress, whereas the late-episode (232–201 Ma) granites were determined to have formed under an extensional setting (Wang et al., 2007, 2013; Yu et al., 2007; Zhao et al., 2013b). In fact, a lot of researches have demonstrated that the extensional setting is favorable for mineralization and can be responsible for the Mesozoic large-scale W, Sn, Cu, Mo, and Au mineralization in South China (e.g., Hou et al., 2013; Mao et al., 2013, 2020). Notably, the compiled mineralization age in this study suggested that the Triassic W, Sn, Nb, Ta, Mo, and Cu mineralization events in South China were predominantly concentrated at 231–206 Ma (**Figure 11B**), synchronous with the late episode (232–201 Ma) magmatism. Thus, the studied Mengshan granites (formed at 226.6–225.9 Ma; **Figure 4**) also have the potential for mineralization.

(2) As discussed above, the studied Mengshan granites were derived from the partial melting of Proterozoic metamorphic basements. In fact, the Proterozoic metamorphic basements in South China, especially the Proterozoic volcanic–sedimentary sequences in the Jiangnan Orogen, were enriched in ore-forming metals, with W, Sn, Cu, and Mo contents reaching 11.8, 5.1, 3.1,

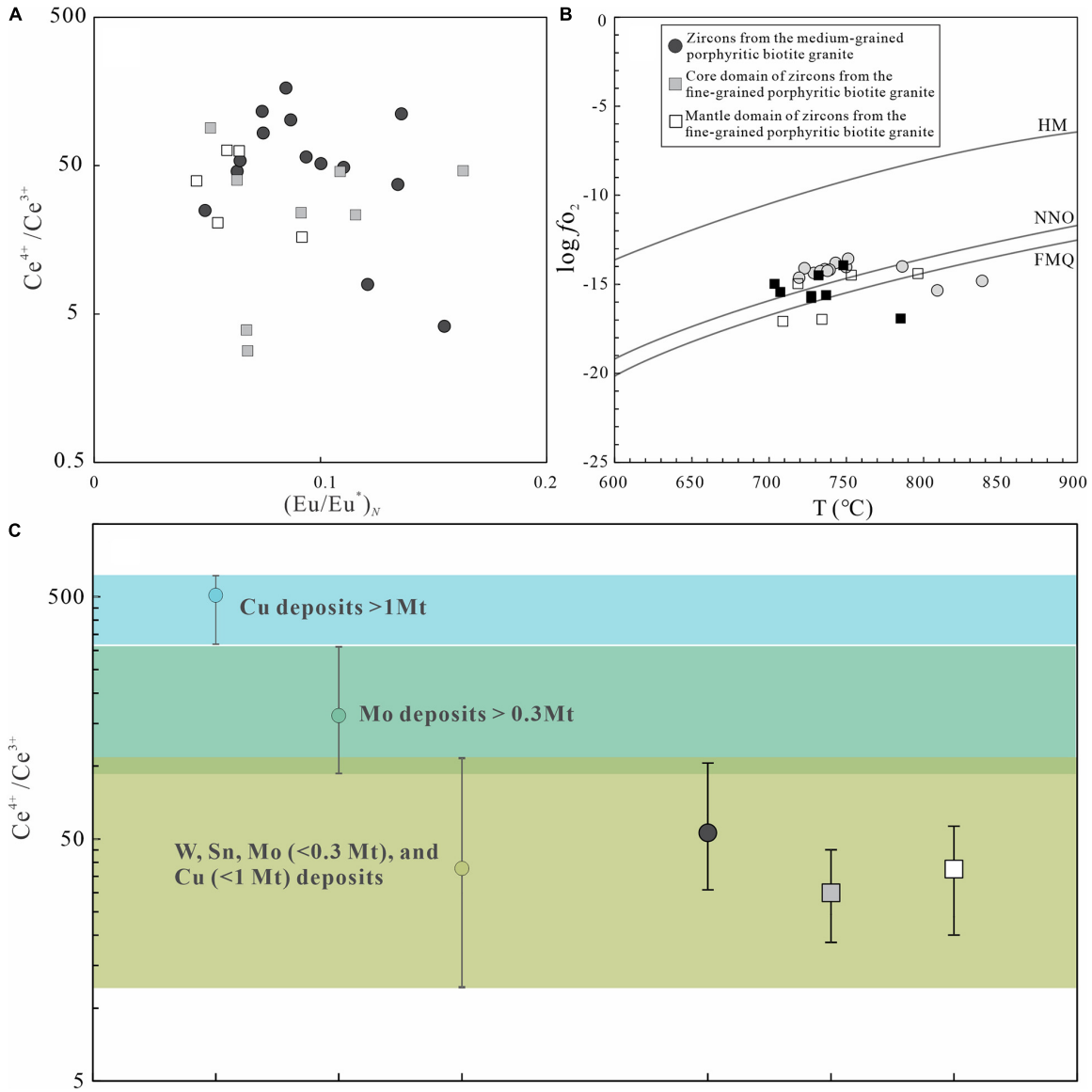

FIGURE 14 | Diagrams of **(A)** zircon Ce^{4+}/Ce^{3+} vs. Eu_N/Eu_N^* and **(B)** logfO_2 vs. Ti-in-zircon temperature for the studied Mengshan granites; **(C)** Comparison of zircon Ce^{4+}/Ce^{3+} ratios of the studied Mengshan granites and the W–Sn, Mo, and Cu deposits. The range of zircon Ce^{4+}/Ce^{3+} ratios from the W–Sn, Mo, and Cu deposits in **(C)** was modified after Yang et al. (2021).

and 45.6 ppm, respectively (Liu and Ma, 1982; Xu, 1988; Chi et al., 2012). Consequently, partial melting of the fertile metamorphic basements leads to the initial enrichment of ore-forming elements and is favorable for mineralization.

(3) The existence of F in magma has been experimentally proven to extend the magmatic evolutionary process and enhance the efficacy of melt segregation and crystal-melt fractionation (Linnen, 1998), leading to the enrichment of ore-forming metals (Hedenquist and Lowenstern, 1994; Wu et al., 2017; Pan et al., 2018). In this study, fluorite was observed to occur as inclusions in feldspar in the fine-grained porphyritic biotite granite (**Figure 3E**), and fluorite can also occur as euhedral grains or as veins in the contact zone between the fine-grained porphyritic biotite granite and Permian carbonate rocks (**Figure 3F**), suggesting the enrichment of F in the granitic system. Correspondingly, whole-rock geochemistry and zircon composition indicated that the fine-grained porphyritic biotite granite was a highly evolved granite. A previous study suggested that the zircon crystallized from highly evolved granites can incorporate up to mass% of W, Sn, Nb, and Ta (Pettke et al., 2005). In this study, the relatively elevated contents of Nb and Ta in zircons from the medium-grained porphyritic biotite granite (mean values of 5.73 and 2.88, respectively; **Supplementary Table 2**) to the fine-grained porphyritic biotite granite (mean values of

7.52 and 4.53, respectively) might also indicate W and Sn enrichment in the granite melts.

The prolonged magmatic evolution of the highly evolved granites is commonly accompanied by intense melt–fluid interactions, because F enrichment in granitic melts can increase the solubility of the fluid, leading to the coexistence of melt and fluid (Bau, 1996; Jahn et al., 2001). This process is favorable for the mobilization, enrichment, and precipitation of ore-forming metals (e.g., Hulsbosch et al., 2016; Lecumberri-Sanchez et al., 2017); thus, it is crucial for metal mineralization. Based on the above discussions, the studied Mengshan granites, especially the fine-grained porphyritic biotite granite, exhibited non-charge-and-radius-controlled trace element behavior, for example, low K/Rb, Nb/Ta, and Zr/Hf ratios, suggesting the existence of melt–fluid interaction. Moreover, zircons from the fine-grained porphyritic biotite granite showed metasomatized rims, also indicating that the granite experienced melt–fluid interaction. Ballouard et al. (2016) suggested that whole-rock Zr/Hf and Nb/Ta values of 18–46 and <5, respectively, can be considered as possible indicators of Sn–W–(U)-related granites. The studied Mengshan granites exhibited low Zr/Hf and Nb/Ta ratios (**Supplementary Table 3**), with some of the samples plotted in the range of Sn–W–(U)-related granites (**Figure 13B**), indicating that they have potential for Sn–W–(U) mineralization.

(4) The magmatic redox state can play an important role in determining the types of ore deposits produced from magmatic melts by affecting the enrichment processes of the metals. The oxidized state of magmatic melts can suppress the premature precipitation of Cu-bearing sulfides and is beneficial for the enrichment of Cu during magmatic differentiation (Jugo, 2009). The oxidized state is also beneficial for Mo enrichment, because Mo occurs mainly as Mo^{6+} under oxidized conditions and thus prefers to remain in the residual melt until it is scavenged by magmatic aqueous fluids rather than occurring as Mo^{4+} to substitute for Ti^{4+} (0.61 Å) in Ti-bearing mineral phases (Candela and Bouton, 1990). In contrast, a reduced state is beneficial for Sn enrichment, as Sn occurs primarily as Sn^{2+} under reduced conditions and prefers to remain in the residual melt (Linnen et al., 1996). Therefore, porphyry–skarn-type Cu and Mo deposits, especially the super-large ones, are generally associated with more oxidized magmas. Meanwhile, the granite-related Sn deposits are commonly associated with reduced magmas. The enrichment of W in magma shows little dependence on the magmatic redox state (Kwak and White, 1982). In this study, the Mengshan granites had relatively low Fe_2O_3/FeO ratios (mostly < 0.5; **Supplementary Table 3**), which corresponds to the ilmenite series proposed by Ishihara (1981). Meanwhile, in the diagram of the Fe_2O_3/FeO vs. Rb/Sr ratio (**Figure 13D**), the studied Mengshan granites plotted close to the W- (scheelite) and W–Mo–Sn-related granitoids, indicating that they were related to W, Mo, and Sn mineralization.

Recently, some researchers have found that there is a size–oxidation relationship for porphyry–skarn-type Cu and Mo deposits (Shen et al., 2015; Shu et al., 2019). Specifically, larger porphyry(–skarn) Cu and Mo deposits are generally associated with more oxidized magmas, whereas Cu and Mo in smaller deposits are related to less oxidized (or even reduced) magmas. To identify the redox states of different types of ore deposits, Yang et al. (2021) compiled published zircon Ce^{4+}/Ce^{3+} ratios from W–Sn deposits, Mo deposits with tonnage < 0.3 Mt, Mo deposits with Mo tonnage > 0.3 Mt, Cu deposits with tonnage < 1 Mt, and Cu deposits with tonnage > 1 Mt. By comparison, Cu deposits with tonnage > 1 Mt exhibited the highest Ce^{4+}/Ce^{3+} ratio (mostly ranging from 159 to 592; Yang et al., 2021), followed by Mo deposits with tonnage > 0.3 Mt (mostly ranging from 92 to 289). The Cu deposits with tonnage < 1 Mt, Mo deposits with tonnage < 0.3 Mt, and W–Sn deposits similarly showed low Ce^{4+}/Ce^{3+} ratios that mostly ranged from 29 to 103. The studied Mengshan Triassic granites had zircon Ce^{4+}/Ce^{3+} mostly (interquartile range) lower than 90 (**Figure 14C**), indicating that they were relatively reduced and were more likely to form W–Sn, Mo (<0.3 Mt), and Cu (<1 Mt) deposits rather than super-large-scale Cu and Mo deposits. This result was also consistent with the results obtained by the whole-rock Fe_2O_3/FeO ratio (**Figure 13D**).

In conclusion, the proper tectonic setting, potential fertile protolith, prolonged magmatic evolution, melt–fluid interaction, and relatively reduced magmatic redox state suggested that the fine-grained porphyritic biotite granite has the potential to form W, Sn, Mo (<0.3 Mt), and Cu (<1 Mt) deposits. Non-metal mineralization depends on either abundant hydrothermal fluids or proper host rocks. In the Mengshan district, the contact zone between the fine-grained porphyritic biotite granite (or other Triassic granites) and the Permian Maokou Formation (flint-nodule limestone) is a potential target region for wollastonite prospecting.

In fact, based on a previous study, the Triassic granites from the three stages seem to exhibited similar petrological, mineralogical, and geochemical features (Zhong et al., 2011). Thus, although there is no direct geological evidence between the alteration and mineralization, it cannot entirely exclude the possibility that the second and third stages of Triassic Mengshan granites have the potential to form hydrothermal alteration and mineralization, especially for wollastonite mineralization, which is controlled more on the properties of country rock.

CONCLUSION

The medium- and fine-grained porphyritic biotite granite in the Mengshan district is transitional and the latter was closely related to hydrothermal alteration and mineralization. The LA–ICP–MS zircon U–Pb dating provided the weighted mean ages of 225.9 ± 0.5 and 226.6 ± 0.5 Ma for the medium- and fine-grained porphyritic biotite granite, respectively.

Regarding the whole-rock geochemistry and Nd isotopes, the studied Mengshan granites were highly evolved I-type granites that were derived from the disequilibrium melting of Proterozoic metamorphic basements composed of meta-igneous and metasediments. The melt–fluid interaction also occurred during the formation of more evolved fine-grained porphyritic biotite granite.

The proper tectonic setting, potential fertile protolith, extensive magmatic evolution and melt–fluid interaction, and a relatively reduced magmatic redox state indicated that the fine-grained porphyritic biotite granite has the potential for W, Sn, Mo (<0.3 Mt), and Cu (<1 Mt) deposits. Moreover, the contact zone between the fine-grained porphyritic biotite granite (or other Triassic granites) and the Permian Maokou Formation (flint-nodule limestone) is a potential target region for wollastonite prospecting.

DATA AVAILABILITY STATEMENT

The original contributions presented in the study are included in the article/**Supplementary Material**, further inquiries can be directed to the corresponding author/s.

AUTHOR CONTRIBUTIONS

YY, XP, and ZH designed the research. All the authors participated in the field investigation and contributed to read the manuscript. YY, XP, and YD conducted the analysis work. YY compiled the published data and wrote the manuscript.

FUNDING

This work was financially supported by the China Geological Survey (grant number: DD20190001), the Ministry of Science and Technology of the People's Republic of China (grant number: 2016YFC0600203), and the National Natural Science Foundation of China (grant number: 41873059).

ACKNOWLEDGMENTS

We are grateful to reviewers HL, JL, RZ, JZ, SL, and editor GW for their constructive and helpful suggestions that improved the manuscript. We also thank Sibao Chen, Xuguang Cheng, Shaohua, Liu, and other general staff members from the 224 Geological Team, Bureau of Coalfield Geology of Jiangxi Province for their assistance with the fieldwork.

SUPPLEMENTARY MATERIAL

The Supplementary Material for this article can be found online at: https://www.frontiersin.org/articles/10.3389/feart.2021.657618/full#supplementary-material

Supplementary Figure 1 | Diagrams of LOI vs. major element compositions for the Mengshan Triassic granites.

Supplementary Table 1 | (A–B) Chondrite-normalized REE patterns of zircons from the medium-grained porphyritic biotite granite (MS19–05) and the fine-grained porphyritic biotite granite (SSZK01–123); **(C–D)** Discriminant diagrams for magmatic and hydrothermal zircons (modified after Hoskin, 2005 and Li et al., 2014).

REFERENCES

Ballard, J. R., Pallin, J. M., and Campbell, I. H. (2002). Relative oxidation states of magmas inferred from Ce(IV)/Ce(III) in zircon: application to porphyry copper deposits of northern Chile. *Contribut. Mineral. Petrol.* 144, 347–364. doi: 10.1007/s00410-002-0402-5

Ballouard, C., Poujol, M., Boulvais, P., Branquet, Y., Tartèse, R., and Vigneresse, J. L. (2016). Nb-Ta fractionation in peraluminous granites: a marker of the magmatic-hydrothermal transition. *Geology* 44, 231–234. doi: 10.1130/g37475.1

Bau, M. (1996). Controls on the fractionation of isovalent trace elements in magmatic and aqueous systems: evidence from Y/Ho, Zr/Hf, and lanthanide tetrad effect. *Contribut. Mineral. Petrol.* 123, 323–333. doi: 10.1007/s004100050159

Bea, F., Pereira, M. D., and Stroh, A. (1994). Mineral/leucosome trace-element partitioning in a peraluminous migmatite (a laser ablation-ICP-MS study). *Chem. Geol.* 117, 291–312. doi: 10.1016/0009-2541(94)90133-3

Belousova, E., Griffin, W., O'Reilly, S. Y., and Fisher, N. (2002). Igneous zircon: trace element composition as an indicator of source rock type. *Contribut. Mineral. Petrol.* 143, 602–622. doi: 10.1007/s00410-002-0364-7

Blevin, P. L. (2004). Redox and compositional parameters for interpreting the granitoid metallogeny of eastern Australia: implications for gold-rich ore systems. *Resource Geol.* 54, 241–252. doi: 10.1111/j.1751-3928.2004.tb00205.x

Blundy, J., and Wood, B. (1994). Prediction of crystal-melt partition coefficients from elastic moduli. *Nature* 372, 452–454. doi: 10.1038/372452a0

Boss, A. P. (2008). Mixing in the solar nebula: implications for isotopic heterogeneity and large-scale transport of refractory grains. *Earth Planet. Sci. Lett.* 273, 102–109. doi: 10.1016/j.epsl.2008.01.008

Brown, M. (2013). Granite: from genesis to emplacement. *Geol. Soc. Am. Bull.* 125, 1079–1113. doi: 10.1130/b30877.1

Burnham, C. W. (1979). "Magmas and hydrothermal fluids," in *Geochemistry of Hydrothermal Ore Deposits*, ed. L. H. Barnes (New York, NY: John Wiley & Sons Press), 71–136.

Cai, M. H., Chen, K. X., and Qu, W. J. (2006). Geological characteristics and Re-Os dating of molybdenites in Hehuaping tin-polymetallic deposit, southern Hunan Province. *Miner. Deposits* 25, 263–268.

Candela, P. A., and Bouton, S. L. (1990). The influence of oxygen fugacity on tungsten and molybdenum partitioning between silicate melts and ilmenite. *Econ. Geol.* 85, 633–640. doi: 10.2113/gsecongeo.85.3.633

Carmichael, I. S. E., and Ghiorso, M. S. (1990). The effect of oxygen fugacity on the redox state of natural liquids and their crystallizing phases. *Rev. Mineral. and Geochem.* 24, 191–212.

Černý, P., Blevin, P. L., Cuney, M., and London, D. (2005). Granite-related ore deposits. *Econ. Geol.* 100, 337–370.

Chappell, B. W., Bryant, C. J., and Wyborn, D. (2012). Peraluminous I-type granites. *Lithos* 153, 142–153. doi: 10.1016/j.lithos.2012.07.008

Chappell, B. W., and White, A. J. R. (1992). I- and S-type granites in the Lachlan Fold Belt. *Earth Environ. Sci. Trans. R. Soc. Edinburgh* 83, 1–26.

Chen, C., Chen, S. B., and Cheng, X. G. (2018). Geological characteristics and genesis of a wollastonite mineral deposit in the Shizhushan-Zhangmuqiao, Mengshan area of Jiangxi. *Shanghai Land Resources* 39, 19–24.

Chen, G. H., Zhan, T. W., Wang, X. G., Huang, Q. Y., Yi, W., and Yu, X. (2019). Zircon U-Pb age and significance of metallogenic magmatic rocks in Shizhushan wollastonite deposit, Mengshan district, Jiangxi province. *Geol. Jiangxi* 20, 82–88.

Chen, G. N., and Grapes, R. (2007). *Granite Genesis: in-Situ Melting and Crustal Evolution*. Netherlands: Springer Press.

Chen, J., Lu, J. J., Chen, W. F., Wang, R. C., Ma, D. S., Zhu, J. C., et al. (2008). W-Sn-Nb-Ta-bearing granites in the Nanling range and their relationship to metallogenesis. *Geol. J. China Univ.* 14, 459–473.

Chen, J. F., and Jahn, B. (1998). Crustal evolution of southeastern China: Nd and Sr isotopic evidence. *Tectonophyscis* 284, 101–133. doi: 10.1016/s0040-1951(97)00186-8

Cheng, Y. B., and Mao, J. W. (2010). Age and geochemistry of granites in Gejiu area, Yunnan Province, SW China: constrains on their petrogenesis and corresponding tectonic setting. *Lithos* 120, 258–276. doi: 10.1016/j.lithos.2010.08.013

Chi, Q. H., Wang, X. Q., Xu, S. F., Zhou, J., Liu, H. L., Liu, D. S., et al. (2012). Temporal and spatial distribution of tungsten and tin in South China Continental. *Earth Sci. Front.* 19, 70–83. doi: 10.1016/j.csr.2019.02.001

Couzinié, S., Laurent, O., Moyen, J. F., Zeh, A., Bouilhol, P., and Villaros, A. (2016). Post-collisional magmatism: crustal growth not identified by zircon Hf-O isotopes. *Earth Planet. Sci. Lett.* 456, 182–195. doi: 10.1016/j.epsl.2016.09.033

Deering, C. D., Keller, B., Schoene, B., Bachmann, O., Beane, R., and Ovtcharova, M. (2016). Zircon record of the plutonic-volcanic connection and protracted rhyolite melt evolution. *Geology* 44, 267–270. doi: 10.1130/g37539.1

Dostal, J., and Chatterjee, A. K. (2000). Contrasting behaviour of Nb/Ta and Zr/Hf ratios in a peraluminous granitic pluton (Nova Scotia, Canada). *Chem. Geol.* 163, 207–218. doi: 10.1016/s0009-2541(99)00113-8

Du, Y., Shao, Y. J., Luo, X. Y., Guo, A. M., Huang, G. F., Tian, L., et al. (2015). Geological features and genesis of Tianmuchong polymetallic tungsten-tin deposit in Guiyang Country, Hunan Province. *Geol. Miner. Resourc. South China* 31, 354–367.

Duan, X. X., Chen, B., Sun, K. K., Wang, Z. Q., Yan, X., and Zhang, Z. (2019). Accessory mineral chemistry as a monitor of petrogenetic and metallogenetic processes: a comparative study of zircon and apatite from Wushan Cu- and Zhuxiling W(Mo)-mineralization-related granitoids. *Ore Geol. Rev.* 111:102940. doi: 10.1016/j.oregeorev.2019.102940

Feng, J. R., Mao, J. W., Pei, R. F., and Li, C. (2011). A tentative discussion on Idosinian ore-forming events in Laojunshan area of southeastern Yunnan: a case study of Xinzhai tin deposit and Nanyangtian tungsten deposit. *Miner. Deposits* 30, 57–73.

Feng, M., Feng, Z. H., Kang, Z. Q., Fu, W., Qing, Y., Hu, R. G., et al. (2019). Establishing an Indosinian geochronological framework for episodic granitic emplacement and W-Sn-Nb-Ta mineralization in Limu mining district, South China. *Ore Geol. Rev.* 107, 1–13. doi: 10.1016/j.oregeorev.2019.02.012

Ferry, J. M., and Watson, E. B. (2007). New thermodynamic models and revised calibrations for the Ti-in-zircon and Zr-in-rutile thermometers. *Contribut. Mineral. Petrol.* 154, 429–437. doi: 10.1007/s00410-007-0201-0

Gao, P., Zheng, Y. F., and Zhao, Z. F. (2016). Experimental melts from crustal rocks: a lithochemical constraint on granite petrogenesis. *Lithos* 266–267, 133–157. doi: 10.1016/j.lithos.2016.10.005

Geisler, T., Schaltegger, U., and Tomaschek, F. (2007). Re-equlibration of zircon in aqueous fluids and melts. *Elements* 3, 43–50. doi: 10.2113/gselements.3.1.43

Guo, F., Fan, W. M., Lin, G., and Lin, Y. X. (1997). Sm-Nd dating and petrogenesis of Mesozoic gabbro xenolith in Daoxian County, Hunan Province. *Chin. Sci. Bull.* 42, 1661–1663.

Harrison, T. M., and Watson, E. B. (1984). The behavior of apatite during crustal anatexis, equilibrium and kinetic considerations. *Geochim. Cosmochim. Acta* 48, 1467–1477. doi: 10.1016/0016-7037(84)90403-4

Hedenquist, J. W., and Lowenstern, J. B. (1994). The role of magmas in the formation of hydrothermal ore deposits. *Nature* 370, 519–527. doi: 10.1038/370519a0

Hoskin, P. W. O. (2005). Trace-element composition of hydrothermal zircon and the alteration of Hadean zircon from the Jack Hills, Australia. *Geochim. Cosmochim. Acta* 69, 637–648. doi: 10.1016/j.gca.2004.07.006

Hou, K. J., Li, Y. H., and Xie, G. Q. (2007). Laser ablation-MC-ICP-MS technique for Hf isotope microanalysis of zircon and its geological applications. *Acta Petrol. Sin.* 23, 2595–2604.

Hou, Z. Q., Pan, X. F., Li, Q. Y., Yang, Z. M., and Song, Y. C. (2013). The giant Dexing porphyry Cu-Mo-Au deposit in east China: product of melting of juvenile lower crust in an intracontinental setting. *Miner. Deposita* 48, 1019–1045. doi: 10.1007/s00126-013-0472-5

Hua, R. M., and Mao, J. W. (1999). A preliminary discussion on the Mesozoic metallogenic explosion in east China. *Miner. Deposits* 18, 300–307.

Huang, H., Niu, Y. L., Teng, F. Z., and Wang, S. J. (2019). Discrepancy between bulk-rock and zircon Hf isotopes accompanying Nd-Hf isotope decoupling. *Geochim. Cosmochim. Acta* 259, 17–36. doi: 10.1016/j.gca.2019.05.031

Huang, L. C., and Jiang, S. Y. (2014). Highly fractionated S-type granites from the giant Dahutang tungsten deposit in Jiangnan Orogen, Southeast China: geochronology, petrogenesis and their relationship with W-mineralization. *Lithos* 202–203, 207–226. doi: 10.1016/j.lithos.2014.05.030

Hulsbosch, N., Boiron, M., Dewaele, S., and Muchez, P. (2016). Fluid fractionation of tungsten during granite-pegmatite differentiation and the metal source of peribatholitic W quartz veins: evidence from the Karagwe-Ankole Belt (Rwanda). *Geochim. Cosmochim. Acta* 175, 299–318. doi: 10.1016/j.gca.2015.11.020

Ishihara, S. (1981). The granitoids series and mineralization. *Econ. Geol.* 75, 458–484.

Jahn, B., Wu, F. Y., Capdevila, R., Martineau, F., Zhao, Z. H., and Wang, Y. X. (2001). Highly evolved juvenile granites with tetrad REE patterns: the Woduhe and Baerzhe granites from the Great Xing'an Mountains in NE China. *Lithos* 59, 171–198. doi: 10.1016/s0024-4937(01)00066-4

Jiang, H., Jiang, S. Y., Li, W. Q., Zhao, K. D., and Peng, N. J. (2018). Highly fractionated Jurassic I-type granites and related tungsten mineralization in the Shirenzhang deposit, northern Guangdong, South China: evidence from cassiterite and zircon U-Pb ages, geochemistry and Sr-Nd-Pb-Hf isotopes. *Lithos* 312–313, 186–203. doi: 10.1016/j.lithos.2018.04.030

Jiang, S. Y., Zhao, K. D., Jiang, H., Su, H. M., Xiong, S. F., Xiong, Y. Q., et al. (2020). Spatiotemporal distribution, geological characteristics and metallogenic mechanism of tungsten and tin deposits in China: an overview. *Chin. Sci. Bull.* 65, 3730–3745.

Jiang, W. C., Li, H., Evans, N. J., and Wu, J. H. (2019). Zircon records multiple magmatic -hydrothermal process at the giant Shizhuyuan W-Sn-Mo-Bi polymetallic deposit, South China. *Ore Geol. Rev.* 115:103160. doi: 10.1016/j.oregeorev.2019.103160

Jiang, Y. H., Zhao, P., Zhou, Q., Liao, S. Y., and Jin, G. D. (2011). Petrogenesis and tectonic implications of Early Cretaceous S- and A-type granites in the northwest of the Gan-Hang rift, SE China. *Lithos* 121, 55–73. doi: 10.1016/j.lithos.2010.10.001

Jiang, Y. H., and Zhu, S. Q. (2017). Petrogenesis of the Late Jurassic peraluminous biotite granites and muscovite-bearing granites in SE China: geochronological, elemental and Sr-Nd-O-Hf isotopic constraints. *Contribut. Mineral. Petrol.* 172:101.

Jugo, P. J. (2009). Sulfur content at sulfide saturation in oxidized magmas. *Geology* 37, 415–418. doi: 10.1130/g25527a.1

Jung, S., Hoernes, S., and Mezger, K. (2000). Geochronology and petrogenesis of Pan-African, syn-tectonic, S-type and post-tectonic A-type granite (Namibia): products of melting of crustal sources, fractional crystallization and wall rock entrainment. *Lithos* 50, 259–287. doi: 10.1016/s0024-4937(99)00059-6

King, P. L., White, A. J. R., Chappell, W., and Allen, C. M. (1997). Characterization and origin of aluminous A-type granites from the Lachlan Fold Belt, Southeastern Australian. *J. Petrol.* 38, 371–391. doi: 10.1093/petroj/38.3.371

Kwak, T. A. P., and White, A. J. R. (1982). Contrasting W-Mo-Cu and W-Sn-F skarn types and related granitoids. *Min. Geol.* 32, 339–351.

Large, S. J. E., Quadt, A., Wotzlaw, J. F., Guilong, M., and Heinrich, C. A. (2018). Magma evolution leading to porphyry Au-Cu mineralization at the Ok Tedi deposit, Papua igneous Guina: trace element geochemistry and high-precision geochronology of igneous zircon. *Econ. Geol.* 113, 39–61. doi: 10.5382/econgeo.2018.4543

Lecumberri-Sanchez, P., Vieira, R., Heinrich, C. A., Pinto, F., and Wälle, M. (2017). Fluid-rock interaction is decisive for the formation of tungsten deposits. *Geology* 45, 579–582. doi: 10.1130/G38974.1

Lee, R. G., Byrne, K., D'Angelo, M., Hart, C. J. R., Hollings, P., Gleeson, S. A., et al. (2020). Using zircon trace element composition to assess porphyry copper potential of the Guichon Creek batholith and Highland Valley copper deposit, south-central British Columbia. *Miner. Deposita* 56, 215–238. doi: 10.1007/s00126-020-00961-1

Lee, R. G., Dilles, J. H., Tosdal, R. M., Wooden, J. L., and Mazdab, F. K. (2017). Magmatic evolution of granodiorite intrusions at the EI Salvador porphyry

copper deposit, Chile, based on trace element composition and U/Pb age of zircons. *Econ. Geol.* 112, 245–273. doi: 10.2113/econgeo.112.2.245

Li, C. L., Wang, Z. X., Lv, Q. T., Tan, Y. L., Li, L. L., and Tao, T. (2021). Mesozoic tectonic evolution of the eastern South China block: a review on the synthesis of the regional deformation and magmatism. *Ore Geol. Rev.* 131:104028. doi: 10.1016/j.oregeorev.2021.104028

Li, H., Watanabe, K., and Yonezu, K. (2014). Zircon morphology, geochronology and trace element geochemistry of the granites from the Huangshaping polymetallic deposit, South China: Implications for the magmatic evolution and mineralization process. *Ore Geol. Rev.* 60, 14–35. doi: 10.1016/j.oregeorev.2013.12.009

Li, H., Wu, J. H., Evans, N. J., Jiang, W. C., and Zhou, Z. K. (2018). Zircon geochronology and geochemistry of the Xianghualing A-type granitic rocks: Insights into multi-stage Sn-polymetallic mineralization in South China. *Lithos* 312–313, 1–20. doi: 10.1016/j.lithos.2018.05.001

Li, J., Huang, X. L., He, P. L., Li, W. X., Yu, Y., and Chen, L. L. (2015). In situ analyses of micas in the Yashan granite, South China: constraints on magmatic and hydrothermal evolutions of W and Ta-Nb bearing granites. *Ore Geol. Rev.* 65, 793–810. doi: 10.1016/j.oregeorev.2014.09.028

Li, W. K., Cheng, Y. Q., and Yang, Z. M. (2019). Geo-fO_2: intergrated software for analysis of magmatic oxygen fugacity. *Geochem. Geophys. Geosyst.* 20, 2542–2555.

Li, X. C., Yang, K. F., Spandler, C., Fan, H. R., Zhou, M. F., Hao, J. L., et al. (2021). The effect of fluid-aided modification on the Sm-Nd and Th-Pb geochronology of monazite and bastnäsite: implication for resolving complex isotopic age data in REE ore system. *Geochim. Cosmochim. Acta* 300, 1–24. doi: 10.1016/j.gca.2021.02.028

Li, X. F., Feng, Z. H., Xiao, R., Song, C. A., Yang, F., Wang, C. Y., et al. (2012). Spatial and temporal distributions and the geological setting of the W-Sn-Mo-Nb-Ta deposits at the northeast Guangxi, South China. *Acta Geol. Sin.* 86, 1713–1725.

Li, X. H., Li, Z. X., Li, W. X., Liu, Y., Yuan, C., Wei, G. J., et al. (2007). U-Pb zircon, geochemical and Sr-Nd-Hf isotopic constraints on age and origin of Jurassic I- and A-type granites from central Guangdong, SE China: a major igneous event in response to foundering of a subducted flat-slab? *Lithos* 96, 186–204. doi: 10.1016/j.lithos.2006.09.018

Lin, J., Liu, Y. S., Yang, Y. H., and Hu, Z. C. (2016). Calibration and correction of LA-ICP-MS and LA-MS-ICP-MS analyses for element contents and isotopic ratios. *Solid Earth Sci.* 1, 5–27. doi: 10.1016/j.sesci.2016.04.002

Linnen, R. L. (1998). The solubility of Nb-Ta-Zr-Hf-W in granitic melts with Li and Li + F: constraints for mineralization in rare metal granites and pegmatites. *Econ. Geol.* 93, 1013–1025. doi: 10.2113/gsecongeo.93.7.1013

Linnen, R. L., and Keppler, H. (2002). Melt composition control of Zr/Hf fractionation in magmatic process. *Geochim. Cosmochim. Acta* 66, 3293–3301. doi: 10.1016/s0016-7037(02)00924-9

Linnen, R. L., Pichavant, M., and Holtz, F. (1996). The combined effects of fO_2 and melt composition on SnO_2 solubility and tin diffusivity in haplogranitic melts. *Geochim. Cosmochim. Acta* 60, 4965–4976. doi: 10.1016/s0016-7037(96)00295-5

Liu, Y. J., and Ma, D. S. (1982). The geochemical studies of tungsten built in South China. *Sci. China Ser. B* 10, 939–950.

London, D., Wolf, M. B., Morgan, G. B., and Garrido, M. G. (1999). Experimental silicate-phosphate equilibria in peraluminous granitic magmas, with a case study of the albuquerque Batholith at Tres Arroyos, Badajoz, Spain. *J. Petrol.* 40, 215–240. doi: 10.1093/petroj/40.1.215

Loucks, R. R., Fiorentini, M. L., and Heneiquez, G. J. (2020). New magmatic oxybarometer using trace elements in zircon. *J. Petrol.* 61, 1–30.

Lu, Y. J., Loucks, R. R., Fiorentini, M. L., McCuaig, T. C., Evans, N. J., Yang, Z. M., et al. (2016). Zircon compositions as a pathfinder for porphyry Cu ± Mo ± Au mineral deposits. *Soc. Econ. Geol. Spec. Public.* 19, 329–347.

Mao, J. W., Chen, Y. B., Cheng, M. H., and Franco, P. (2013). Major types and time-space distribution of Mesozoic ore deposits in South China and their geodynamic settings. *Miner. Deposita* 48, 1019–1045.

Mao, J. W., Ouyang, H. G., Song, S. W., Sanntosh, M., Yuan, S. D., Zhou, Z. H., et al. (2020). Geology and metallogeny of tungsten and tin deposits in China. *Soc. Econ. Geol. Spec. Public.* 22, 411–482.

Mao, J. W., Xiong, B. K., Liu, J., Pirajno, F., Cheng, Y. B., Ye, H. S., et al. (2017). Molybdenite Re/Os dating, zircon U-Pb age and geochemistry of granitoids in the Yangchuling porphyry W-Mo deposit (Jiangnan tungsten ore belt), China: implications for petrogenesis, mineralization and geodynamic setting. *Lithos* 286–287, 35–52. doi: 10.1016/j.lithos.2017.05.023

Nash, W. P., and Crecraft, H. R. (1985). Partition coefficients for trace elements in silicic magmas. *Geochim. Cosmochim. Acta* 49, 2309–2322. doi: 10.1016/0016-7037(85)90231-5

Nathwani, C. L., Simmons, A. T., Large, S. J. E., Wilkinson, J. J., Buret, Y., and Lhlenfeld, C. (2021). From long-lived batholith construction to giant porphyry copper deposit formation: petrological and zircon chemical evolution of the Quellaveco district, Southern Peru. *Contribut. Mineral. Petrol.* 176:12.

Ni, P., Wang, G. G., Li, W. S., Chi, Z., Li, S. N., and Gao, Y. (2021). A review of the Yanshanian ore-related felsic magmatism and tectonic settings in the Nanling W-Sn and Wuyi Au-Cu metallogenic belts, Cathaysia Block, South China. *Ore Geol. Rev.* 133:104088. doi: 10.1016/j.oregeorev.2021.104088

Pan, X. F., Hou, Z. Q., Zhao, M., Chen, G. H., Rao, J. F., Li, Y., et al. (2018). Geochronology and geochemistry of the granites from the Zhuxi W-Cu ore deposit in South China: implication for petrogenesis, geodynamical setting and mineralization. *Lithos* 30, 155–179. doi: 10.1016/j.lithos.2018.01.014

Patiño Douce, A. E. (1999). What do experiments tell us about the relative contributions of crust and mantle to the origin of granitic magmas? *Geol. Soc. Lond. Spec. Public.* 168, 55–75. doi: 10.1144/gsl.sp.1999.168.01.05

Paton, C., Woodhead, J. D., Hellstrom, J. C., Hergt, J. M., Greig, A., and Maas, R. (2010). Improved laser ablation U-Pb zircon geochronology through robust downhole fractionation correction. *Geochem. Geophys. Geosyst.* 11, 1–36.

Pettke, T., Audétat, A., Schaltegger, U., and Heinrich, C. A. (2005). Magmatic-to-hydrothermal crystallization in the W-Sn mineralized Mole Granite (NSW, Australia) Part ?: evolving zircon and thorite trace element chemistry. *Chem. Geol.* 220, 191–213. doi: 10.1016/j.chemgeo.2005.02.017

Shaw, D. M. (1968). A review of K-Rb fractionation trends by covariance analysis. *Geochim. Cosmochim. Acta* 32, 573–601. doi: 10.1016/0016-7037(68)90050-1

Shen, P., Hattori, K., Pan, H. D., Jackson, S., and Seitmuratova, E. (2015). Oxidation condition and metal fertility of granitic magmas: zircon trace-element data from porphyry Cu deposits in the central Asian Orogenic Belt. *Econ. Geol.* 110, 1861–1878. doi: 10.2113/econgeo.110.7.1861

Shu, Q. H., Chang, Z. S., Lai, Y., Hu, X. L., Wu, H. Y., Zhang, Y., et al. (2019). Zircon trace elements and magma fertility: insights from porphyry (-skarn) Mo deposits in NE China. *Miner. Deposita* 54, 645–656. doi: 10.1007/s00126-019-00867-7

Stepanov, A., Mavrogenes, A. J., Meffre, S., and Davidson, P. (2014). The key role of mica during igneous concentration of tantalum. *Contrib. Mineral. Petrol.* 167, 499–1009. doi: 10.1007/s00410-014-1009-3

Sun, S. S., and McDonough, W. F. (1989). Chemical and isotopic systematics of oceanic basalts: implications for mantle composition and processes. *Geol. Soc. Lond. Spec. Public.* 42, 313–345. doi: 10.1144/gsl.sp.1989.042.01.19

Sun, T. (2006). A new map showing the distribution of granites in South China and its explanatory notes. *Geol. Bull. China* 25, 332–335.

Sun, T., Zhou, X. M., and Chen, P. R. (2003). Mesozoic strongly peraluminous granites from eastern Nanling range, southern China: petrogenesis and implications for tectonics. *Sci. China Ser. D* 33, 1209–1218.

Sun, W. D., Huang, R. F., Li, H., Hu, Y. B., Zhang, C. C., Sun, S. J., et al. (2015). Porphyry deposits and oxidized magmas. *Ore Geol. Rev.* 65, 97–131. doi: 10.1016/j.oregeorev.2014.09.004

Sylvester, P. J., and Liegeois, J. P. (1998). Post-collisional strongly peraluminous granites. *Lithos* 45, 29–44. doi: 10.1016/s0024-4937(98)00024-3

Tang, M., Wang, X. L., Shu, X. J., Wang, D., Yang, T., and Gopon, P. (2014). Hafnium isotopic heterogeneity in zircons from granitic rocks: geochemical evaluation and modeling of "zircon effect" in crustal anatexis. *Earth Planet. Sci. Lett.* 389, 188–199. doi: 10.1016/j.epsl.2013.12.036

Taylor, R. P., and Fallick, A. R. E. (1997). The evolution of fluorine-rich felsic magmas: source dichotomy, magmatic convergence and the origins of topaz granite. *Terra Nova* 9, 105–108. doi: 10.1111/j.1365-3121.1997.00124.x

Trail, D., Watson, E. B., and Taiby, N. D. (2011). The oxidation state of Hadean magmas and implications for early Earth's atmosphere. *Nature* 480, 79–82. doi: 10.1038/nature10655

Trail, D., Watson, E. B., and Taiby, N. D. (2012). Ce and Eu anomalies in zircon as proxies for the oxidation state of magmas. *Geochim. Cosmochim. Acta* 97, 70–87. doi: 10.1016/j.gca.2012.08.032

Vermeesch, P. (2018). Isoplot R: a free and open toolbox for geochronology. *Geosci. Front.* 9, 224–238.

Vervoort, J. D., and Blichert-Toft, J. (1999). Evolution of the depleted mantle: Hf isotope evidence from juvenile rocks through time. *Geochim. Cosmochim. Acta* 63, 533–556. doi: 10.1016/s0016-7037(98)00274-9

Wang, D., Wang, X. L., Cai, Y., Goldstein, S. L., and Yang, T. (2018). Do Hf isotopes in magmatic zircons represent those of their host rocks. *J. Asian Earth Sci.* 154, 202–212. doi: 10.1016/j.jseaes.2017.12.025

Wang, R., Richards, J. P., Hou, Z. Q., Yang, Z. M., Gou, Z. B., and Dufrane, A. (2014). Increasing magmatic oxidation state from Paleocene to Miocene in the eastern Gangdese Belt, Tibet: implication for collision-related porphyry Cu-Mo±Au mineralization. *Econ. Geol.* 109, 1943–1965. doi: 10.2113/econgeo.109.7.1943

Wang, X., and Pupin, J. P. (1992). Distribution characteristics of trace elements in zircons from granitic rocks. *Sci. Geol. Sin.* 2, 131–140.

Wang, X., and Ren, M. H. (2018). Constraints of hydrothermal and magmatic zircon on the origin of the Yaogangxian tungsten deposit, southern China. *Ore Geol. Rev.* 101, 453–467. doi: 10.1016/j.oregeorev.2018.07.011

Wang, X. G., Hu, Z. H., Yu, X., Chen, G. H., Li, Y. H., Zhan, T. W., et al. (2019). Geological characteristics and prospecting significance of the Shizhushan superlarge wollastonite deposit in Mengshan, west Jiangxi Province. *Acta Geosci. Sin.* 40, 259–264.

Wang, X. L. (2017). Some new research progress and main scientific problems of granitic rocks. *Acta Petrol. Sin.* 33, 1445–1458.

Wang, Y. J., Fan, W. M., Sun, M., Liang, X. Q., Zhang, Y. H., and Peng, T. P. (2007). Geochronological, geochemical and geothermal constraints on petrogenesis of the Indosinian peraluminous granites in the South China Block: a case study in the Hunan Province. *Lithos* 96, 475–502. doi: 10.1016/j.lithos.2006.11.010

Wang, Y. J., Fan, W. M., Zhang, G. W., and Zhang, Y. H. (2013). Phanerozoic tectonics of the South China Block: key observations and controversies. *Gondwana Res.* 23, 1273–1305. doi: 10.1016/j.gr.2012.02.019

Wang, Y. J., Zhang, Y. H., Fan, W. M., Xi, W. X., Guo, F., and Lin, G. (2002). Numerical modeling for generation of Indo-Sinian peraluminous granitoids hunan province: basaltic underplating vs tectonic thickening. *Sci. China* 45, 1042–1056. doi: 10.1360/02yd9102

Watson, E. B., and Harrison, T. M. (1983). Zircon saturation revisited: temperature and composition effects in a variety of crustal magma types. *Earth Planet. Sci. Lett.* 64, 295–304. doi: 10.1016/0012-821x(83)90211-x

Whalen, J. B., Currie, K. L., and Chappell, B. W. (1987). A-type granites: geochemical characteristics, discrimination and petrogenesis. *Contrib. Mineral. Petrol.* 95, 407–419. doi: 10.1007/bf00402202

Wooden, J. L., Mazdab, F. K., Barth, A. P., Miller, C. F., and Lowery, L. E. (2006). Temperatures (Ti) and compositional characteristics of zircon: early observations using high mass resolution on the USGS Stanford SHRIMP. *Geochim. Cosmochim. Acta* 70:A707.

Wu, F. Y., Liu, X. C., Ji, W. Q., Wang, J. M., and Yang, L. (2017). Highly fractionated granites: recognition and research. *Sci. China Earth Sci.* 60, 1201–1219. doi: 10.1007/s11430-016-5139-1

Wu, F. Y., Sun, D. Y., Ge, W. C., Zhang, Y. B., Grant, M. L., Wilde, S. A., et al. (2011). Geochronology of the Phanerozoic granitoids in northeastern China. *J. Asia Earth Sci.* 41, 1–30. doi: 10.1016/j.jseaes.2010.11.014

Wu, J., Liang, H. Y., Huang, W. T., Wang, C. L., Sun, W. D., Sun, Y. L., et al. (2012). Indosinian isotope ages of plutons and deposits in southwestern Miaoershan-Yuechengling, northeastern Guangxi and implications on Indosinian mineralization in South China. *Chin. Sci. Bull.* 57, 1126–1136.

Xiao, Q. X., and Yu, L. (2019). Geological characteristics and prospecting direction of deposits in Mengshan area, Jiangxi Province. *World Nonferr. Metals* 14, 254–255.

Xu, J. (1988). W-bearing sedimentary formations and stratabound W-deposits in Jiangxi Province. *Geol. Prospect.* 10, 12–18.

Yang, F., Li, X. F., Feng, Z. H., and Bai, Y. P. (2009). $^{40}Ar/^{39}Ar$ dating of muscovite from greisenized granite and geological significance in Limu tin deposit. *J. Guilin Univ. Technol.* 29, 21–24.

Yang, W. B., Niu, H. C., Shan, Q., Sun, W. D., Zhang, H., Li, N. B., et al. (2013). Geochemistry of magmatic and hydrothermal zircon from the highly evolved Baerzhe alkaline granite: implications for Zr-REE-Nb mineralization. *Miner. Deposita* 49, 452–470.

Yang, Y. S., Pan, X. F., Hou, Z. Q., and Deng, Y. (2021). Redox states and protoliths of late Mesozoic granitoids in the eastern Jiangnan Orogen: implications for W, Mo, Cu, Sn, and (Au) mineralization. *Ore Geol. Rev.* 2021:104038. doi: 10.1016/j.oregeorev.2021.104038

Yin, R., Wang, R. C., Zhang, A. C., Hu, H., Zhu, J. C., Rao, C., et al. (2013). Extreme fractionation from zircon to hafnon in the Koktokay No. 1 granitic pegmatite, Altai, northwestern China. *Am. Mineral.* 98, 1714–1724. doi: 10.2138/am.2013.4494

You, Z. Y., He, S. F., and Yi, W. P. (2006). Geological characteristics and genesis study of the wollastonite deposit in the Mengshan area, Jiangxi Province. *J. East China Instit. Technol.* Supplement, 116–120.

Yu, C., Yang, Z. M., Zhou, L. M., Zhang, L. L., Li, Z. Q., Zhao, M., et al. (2019). Impact of laser focus on accuracy of U-Pb dating of zircons by LA-ICP-MS. *Miner. Deposits* 38, 21–28.

Yu, J. H., Wang, L. J., Wang, X. L., Qiu, J. S., and Zhao, L. (2007). Geochemistry and geochronology of the Fucheng complex in the southeastern Jiangxi Province, China. *Acta Petrol. Sin.* 23, 1441–1456.

Zhang, C., Santosh, M., Luo, Q., Jiang, S., Liu, L. F., and Liu, D. D. (2019). Impact of residual zircon on Nd-Hf isotope decoupling during sediment recycling in subduction zone. *Geosci. Front.* 10, 241–251. doi: 10.1016/j.gsf.2018.03.015

Zhang, W., Jiang, S. Y., Gao, T. S., Ouyang, Y. P., and Zhang, D. (2020a). The effect of magma differentiation and degassing on ore metal enrichment during the formation of the world-class Zhuxi W-Cu skarn deposit: evidence from U-Pb ages, Hf isotopes and trace elements of zircon, and whole-rock geochemistry. *Ore Geol. Rev.* 127:103801. doi: 10.1016/j.oregeorev.2020.103801

Zhang, W., Lentz, D. R., Thorne, K. G., and Massawe, R. J. R. (2020b). Late Silurian-Early Devonian slab break-off beneath the Canadian appalachians: insights from the Nashwaak Granite, west-central New Brunswick, Canada. *Lithos* 358–359:105393. doi: 10.1016/j.lithos.2020.105393

Zhao, K. D., Jiang, S. Y., Chen, W. F., Chen, P. R., and Ling, H. F. (2013a). Zircon U-Pb chronology and elemental and Sr-Nd-Hf isotope geochemistry of two Triassic A-type granites in South China: implication for petrogenesis and Indosinian transtensional tectonism. *Lithos* 160–161, 292–306. doi: 10.1016/j.lithos.2012.11.001

Zhao, K. D., Li, J. R., Ling, H. F., Chen, P. R., Chen, W. F., and Sun, T. (2013b). Geochronology, geochemistry and petrogenesis of two-stage Indosinian granites from the Xiajiang uranium ore deposit, Jiangxi Province: implication for Indisinian tectonics and genesis of uranium-bearing granites in South China. *Acta Petrol. Sin.* 29, 4349–4361.

Zhong, Y. F., Ma, C. Q., Yu, Z. B., Xu, H. J., Wang, S. M., and Wang, L. X. (2011). U-Pb-Hf isotopes of zircons, geochemistry and genesis of Mengshan granitoids in northwestern Jiangxi Province. *Earth Sci. J. China Univ. Geosci.* 36, 703–720.

Zhou, X. M., Sun, T., Shen, W. Z., Shu, L. S., and Niu, Y. L. (2006). Petrogenesis of Mesozoic granitoids and volcanic rocks in South China: a response to tectonic evolution. *Episodes* 29, 26–33. doi: 10.18814/epiiugs/2006/v29/1/004

Zhu, X., Huang, Z. K., and Rui, Z. Y. (1983). *The Geology of Dexing Porphyry Copper Deposit*. Beijing: Geological Publishing House.

Zhu, Y. T., Li, X. F., Xiao, R., Yu, Y., and Wang, C. Z. (2020). Multistage magmatic-hydrothermal activity and W-Cu mineralization at Jiepai, Guangxi Zhuang autonomous region, South China: constraints from geochronology and Nd-Sr-Hf-O isotopes. *Ore Geol. Rev.* 121:103492. doi: 10.1016/j.oregeorev.2020.103492

Conflict of Interest: The authors declare that the research was conducted in the absence of any commercial or financial relationships that could be construed as a potential conflict of interest.